ESC
European Society
of Cardiology

European Heart Journal (2019) **40**, 3081–3093
doi:10.1093/eurheartj/ehz308

BASIC SCIENCE
Arrhythmia/electrophysiology

RRAD mutation causes electrical and cytoskeletal defects in cardiomyocytes derived from a familial case of Brugada syndrome

Nadjet Belbachir[1,2†], Vincent Portero[1†], Zeina R Al Sayed[1], Jean-Baptiste Gourraud[1,3], Florian Dilasser[1], Laurence Jesel[4], Hongchao Guo[2], Haodi Wu[2], Nathalie Gaborit[1], Christophe Guilluy[5], Aurore Girardeau[1], Stephanie Bonnaud[1,3], Floriane Simonet[1,3], Matilde Karakachoff[1,3], Sabine Pattier[3], Carol Scott[6], Sophie Burel[1], Céline Marionneau[1], Caroline Chariau[7], Anne Gaignerie[7], Laurent David[7,8], Emmanuelle Genin[9], Jean-François Deleuze[10], Christian Dina[1,3], Vincent Sauzeau[1], Gervaise Loirand[1], Isabelle Baró[1], Jean-Jacques Schott[1,3], Vincent Probst[1,3], Joseph C. Wu[2], Richard Redon[1,3‡], Flavien Charpentier[1,3]*‡, and Solena Le Scouarnec[1]*‡

[1]l'institut du thorax, INSERM, CNRS, UNIV Nantes, 8 quai Moncousu, 44007 Nantes cedex 1, France; [2]Division of Cardiovascular Medicine, Department of Medicine, Stanford Cardiovascular Institute, Institute for Stem Cell Biology and Regenerative Medicine, Stanford University School of Medicine, Stanford, CA, USA; [3]l'institut du thorax, CHU Nantes, Nantes, France; [4]CHU Strasbourg, Service de Cardiologie, Strasbourg, France; [5]Institute for Advanced Biosciences, INSERM, CNRS, Grenoble, France; [6]The Wellcome Trust Sanger Institute, Hinxton, Cambridge, UK; [7]INSERM, CNRS, UNIV Nantes, CHU Nantes, SFR François Bonamy, iPSC core facility, Nantes, France; [8]Centre de Recherche en Transplantation et Immunologie UMR 1064, INSERM, UNIV Nantes, Institut de Transplantation Urologie Néphrologie (ITUN), CHU Nantes, Nantes, France; [9]Inserm UMR-1078, CHRU Brest, University Brest, Brest, France; and [10]Centre National de Recherche en Génomique Humaine, Institut de Génomique, CEA, Evry, France

Received 8 November 2017; revised 13 April 2018; editorial decision 26 April 2019; accepted 2 May 2019; online publish-ahead-of-print 21 May 2019

See page 3094 for the editorial comment on this article (doi: 10.1093/eurheartj/ehz448)

Aims The Brugada syndrome (BrS) is an inherited cardiac disorder predisposing to ventricular arrhythmias. Despite considerable efforts, its genetic basis and cellular mechanisms remain largely unknown. The objective of this study was to identify a new susceptibility gene for BrS through familial investigation.

Methods and results Whole-exome sequencing performed in a three-generation pedigree with five affected members allowed the identification of one rare non-synonymous substitution (p.R211H) in *RRAD*, the gene encoding the RAD GTPase, carried by all affected members of the family. Three additional rare missense variants were found in 3/186 unrelated index cases. We detected higher levels of *RRAD* transcripts in subepicardium than in subendocardium in human heart, and in the right ventricle outflow tract compared to the other cardiac compartments in mice. The p.R211H variant was then subjected to electrophysiological and structural investigations in human cardiomyocytes derived from induced pluripotent stem cells (iPSC-CMs). Cardiomyocytes derived from induced pluripotent stem cells from two affected family members exhibited reduced action potential upstroke velocity, prolonged action potentials and increased incidence of early afterdepolarizations, with decreased Na^+ peak current amplitude and increased Na^+ persistent current amplitude, as well as abnormal distribution of actin and less focal adhesions, compared with intra-familial control iPSC-CMs Insertion of p.R211H-*RRAD* variant in control iPSCs by genome editing confirmed these results. In addition, iPSC-CMs from affected patients exhibited a decreased L-type Ca^{2+} current amplitude.

---

* Corresponding author. Tel: +33 228 08 00 55, Email: solena.lescouarnec@univ-nantes.fr; Tel: +33 228 08 01 64, Email: flavien.charpentier@univ-nantes.fr

† These authors are co-first authors.

‡ These authors are co-last authors.

Conclusion This study identified a potential new BrS-susceptibility gene, *RRAD*. Cardiomyocytes derived from induced pluripotent stem cells expressing *RRAD* variant recapitulated single-cell electrophysiological features of BrS, including altered Na^+ current, as well as cytoskeleton disturbances.

Keywords Brugada syndrome • RAD GTPase • Induced pluripotent stem cells • Sodium current • L-type calcium current • Actin cytoskeleton

Translational perspective

The Brugada syndrome (BrS) is an inherited cardiac disorder predisposing to ventricular arrhythmias and sudden cardiac death. In a large family affected by BrS, we identified a rare missense mutation in *RRAD*, the gene encoding the RAD GTPase. The mutation leads to electrical and structural defects consistent with BrS in cardiomyocytes differentiated from induced pluripotent stem cells of the family proband. A small but significant excess burden of rare missense variants in *RRAD* was found in unrelated BrS patients, suggesting that *RRAD* may be a new susceptibility gene for BrS.

Introduction

The Brugada syndrome (BrS) is a rare inherited disorder characterized by a specific but labile pattern at the electrocardiogram (ECG), i.e. a coved ST-segment elevation followed by a negative T wave in the right precordial leads, revealing electrical dysfunctions that predispose to ventricular arrhythmias and sudden cardiac death (SCD).[1,2] Despite numerous studies over the last 25 years, the molecular basis for the ECG abnormalities and the mechanism underlying ventricular arrhythmias and SCD in the context of BrS are still incompletely understood.

Mutations in the *SCN5A* gene, which encodes the main cardiac Na^+ channel α-subunit Nav1.5, are found in 20–25% of BrS probands.[3,4] These mutations result in a reduction of the cardiac Na^+ current (I_{Na}) and are thought to decrease rapid cardiomyocyte depolarization and cardiac conduction, a mechanism that may play a key role in BrS pathogenesis.[5] Other rare variants have been reported as predisposing to BrS, affecting more than 20 genes encoding proteins either involved in Nav1.5 regulation, or encoding L-type Ca^{2+} channel subunits and K^+ channels subunits mainly involved in $I_{K,ATP}$ and I_{to} generation.[6,7] However, these additional variants account for <5% of cases, bringing the molecular diagnosis success rate to only 25–30% of cases.

Apart from *SCN5A*, the genes associated with BrS susceptibility have been identified only in few unrelated patients or in small families and often through candidate gene approaches: there is increasing evidence that they may play only a minor role, if any, in the phenotype of the patients.[8–10] Moreover, extended familial genetic investigations revealed numerous occurrences of phenocopies and non-penetrance for the identified familial *SCN5A* variants in families affected by BrS, questioning the autosomal dominant transmission pattern initially proposed.[11] Recently, the identification of three risk loci for BrS by genome-wide association study confirmed a more complex pattern of disease transmission.[12] Despite this genetic complexity, studies on familial cases remain useful to discover new genes involved in disease susceptibility and understand better the pathogenesis of BrS.

In the present study, by applying a whole-exome sequencing approach to a large pedigree with BrS and documented history of SCD, we identified a rare non-synonymous variant (p.R211H) in the *RRAD* gene, which encodes the RAD (Ras Associated with Diabetes) GTPase.[13] We then demonstrated RAD involvement in BrS pathogenesis based on functional studies in cardiomyocytes differentiated from (i) induced pluripotent stem cells (iPSC-CMs) obtained from four family members, two affected members, including the proband, and two unaffected members, and (ii) an isogenic pair of wild type and p.R211H-*RRAD* iPSC-CMs generated from one control individual with independent genetic background. The results were further confirmed in neonatal mouse cardiomyocytes with adenoviral-mediated expression of wild type and p.R211H RAD transcripts.

Methods

The study was conducted according to the principles set forth under the Declaration of Helsinki (1989) and European guidelines for clinical and genetic research. Institutional review board approvals of the study were obtained before the initiation of patient enrolment. Informed written consent was obtained from each patient who agreed to participate in the clinical and genetic study. H9 human embryonic stem cells were used as positive controls for human iPSC characterization under agreement n°RE13-004 from the *Agence de la Biomédecine*.

All the experimental procedures performed in the context of this study are available in detail in the Supplementary material online.

Results

Clinical report: a familial case of Brugada syndrome

The index case (individual III:2; *Figure 1*), a 41-year-old man, was first diagnosed after a systematic ECG. He presented a typical but labile BrS Type I ECG pattern (*Figure 1A*). He mentioned that he had previously experienced palpitations associated with near syncope and

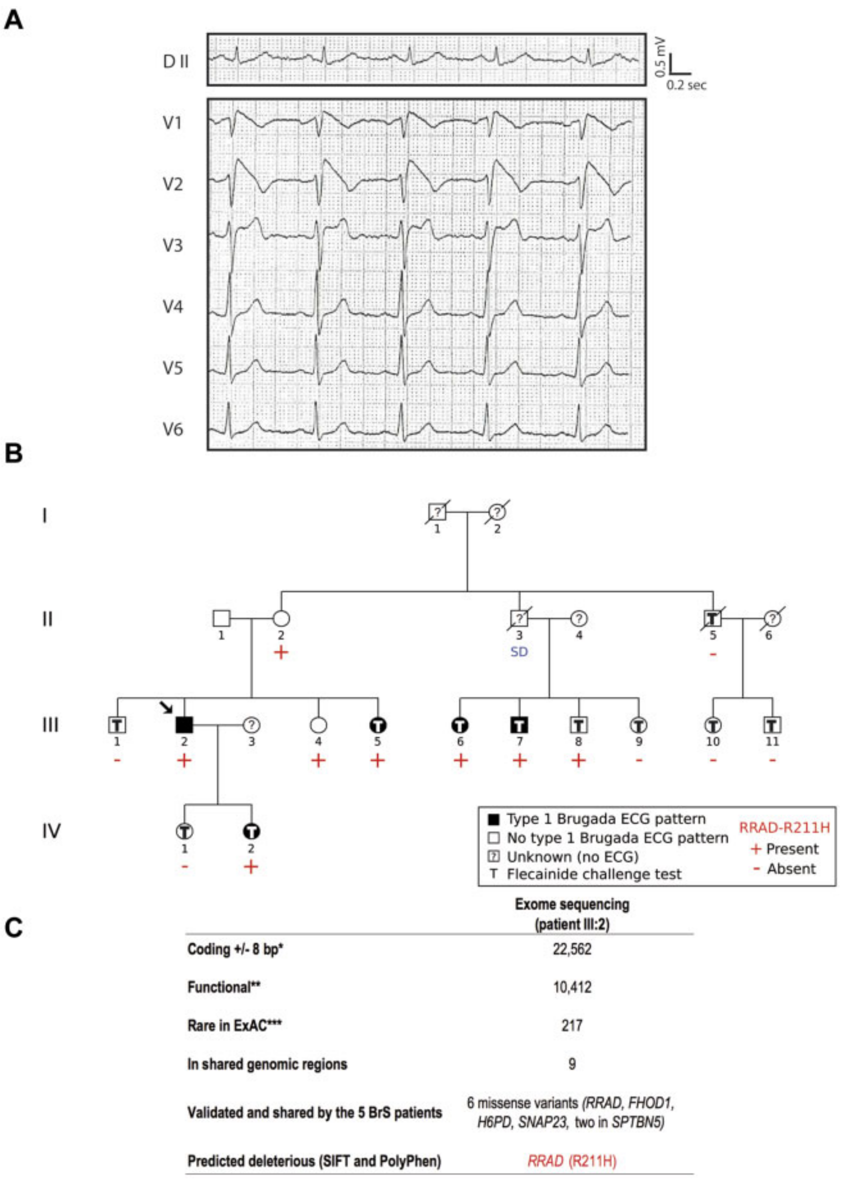

	Exome sequencing (patient III:2)
Coding +/- 8 bp*	22,562
Functional**	10,412
Rare in ExAC***	217
In shared genomic regions	9
Validated and shared by the 5 BrS patients	6 missense variants (*RRAD*, *FHOD1*, *H6PD*, *SNAP23*, two in *SPTBN5*)
Predicted deleterious (SIFT and PolyPhen)	*RRAD* (R211H)

Figure 1 Electrocardiographic pattern and genetic investigation in a family with Brugada syndrome. (*A*) DII peripheral lead and V1–V6 precordial leads of the proband (III:2) under baseline condition. (*B*) Family pedigree. The arrow indicates the proband. Electrocardiograms were recorded in 14 individuals, under baseline conditions only for three individuals (II:1, II:2, and III:4), or under baseline conditions and during flecainide challenge for 11 individuals. DNA was collected for 14 individuals. (*C*) Exome filters. *SO terms (VEP): stop_gained, stop_lost, frameshift_variant, missense_variant, splice_donor_variant, splice_acceptor_variant, initiator_codon_variant, inframe_insertion, inframe_deletion, splice_region_variant, synonymous_variant, and stop_retained_variant. **SO terms (VEP): stop_gained, stop_lost, frameshift_variant, missense_variant, splice_donor_variant, splice_acceptor_variant, initiator_codon_variant, inframe_insertion, and inframe_deletion. ***MAF (Minor Allele Frequency) <0.1% in all ExAC populations. SD, sudden death.

nocturnal agonal respiration. After implantable cardioverter-defibrillator implantation, neither recurrent symptoms nor ventricular arrhythmias have been observed. During familial screening, four relatives were identified as affected after flecainide challenge (*Figure 1B*). In addition, individual III:8 exhibited a BrS Type II ECG pattern under flecainide (Supplementary material online, *Figure S1*). None of these individuals had presented relevant symptoms. However, an unexplained sudden death occurred at rest in a 41-year-old proband's uncle (individual II:3). Electrocardiogram and clinical parameters for this French family are provided in *Table 1*.

Identification of a rare *RRAD* variant in a familial case of Brugada syndrome

Whole-exome sequencing on the index case unveiled 217 rare coding variants (Supplementary material online, *Methods*). After analysing

Table 1 Electrocardiogram and clinical parameters of the family members

Family members	*Chr16* haplotype	Type I ECG pattern	Baseline RR (ms)	Baseline P (ms)	Baseline PR (ms)	Baseline QRS (ms)	Baseline QTc (ms)	Baseline TPE (ms)	Flecainide RR (ms)	Flecainide P (ms)	Flecainide PR (ms)	Flecainide QRS (ms)	Flecainide QTc (ms)	Flecainide TPE (ms)
III:2	Yes	Spontaneous	828	98	165	100	410	72	—	—	—	—	—	—
III:5	Yes	Drug induced	942	90	139	97	410	59	955	87	160	104	438	67
III:6	Yes	Drug induced	1015	76	145	133	426	67	949	72	144	149	447	72
III:7	Yes	Drug induced	711	108	152	118	395	67	872	106	196	127	402	66
III:8	Yes	No[a]	724	81	152	91	375	22	755	95	196	95	385	51
IV:2	Yes	Drug induced	617	83	122	88	409	64	649	87	157	116	464	52
II:5	No	No	882	117	200	101	424	69	829	109	217	113	427	68
III:1	No	No	1262	112	204	89	339	55	986	115	206	119	407	63
III:9	No	No	832	82	158	89	394	61	849	103	206	99	439	100
III:10	No	No	938	93	166	91	358	52	942	100	204	90	385	59
III:11	No	No	928	97	177	104	397	73	867	111	221	107	405	70
IV:1	No	No	897	93	148	87	375	62	679	103	162	103	446	118

P, P wave; PR, PR interval; QRS, QRS complex, QTc, corrected QT interval; TPE, time interval between the peak and the end of the T wave.

[a] Type II ECG pattern under flecainide (Supplementary material online, *Figure S1*).

variants located in genomic regions shared by all affected family members and co-segregation analyses, six missense variants were detected in all five affected patients (*Figure 1C*). They were located in *RRAD* and *FHOD1* on chromosome 16, *H6PD* on chromosome 1, and *SNAP23* and *SPTBN5* (two variants) on chromosome 15 (Supplementary material online, *Table S1*). While there were six non-affected carriers for each variant on chromosomes 1 and 15, both variants located on chromosome 16 (in *RRAD* and *FHOD1*) were carried by only three non-affected relatives (Supplementary material online, *Table S1*; *Figure 1B*): the individual III:8 presenting with a BrS Type II ECG pattern, and two women (II:2 and III:4) for whom drug challenge could not be performed. Furthermore, among the six missense variants, the *RRAD* variant (p.Arg211His) was the only one predicted to be damaging by SIFT and PolyPhen-2 tools (Supplementary material online, *Tables S1* and *S2*). This variant is also associated to the highest CADD score (CADD PHRED score: 33) and is currently reported as the least frequent in the gnomAD database (1/242 446 alleles; Supplementary material online, *Table S1*). By screening the four coding exons of *RRAD* in 186 unrelated BrS patients using Sanger sequencing, we identified three additional rare missense mutations in isolated cases: p.Asp46Tyr, p.Gln186Arg, and p.Val215Met (Supplementary material online, *Table S2*). Overall, we detected a trend for enrichment ($P = 0.042$, odds ratio = 6.98, 95% confidence interval: 0.79–84.33) in rare *RRAD* non-synonymous variants (with a MAF below 0.1% in gnomAD) among the BrS cases (three carriers out of 186 cases) compared to a population of 856 reference individuals of French origin, for which *RRAD* genotype status was available in-house (2 carriers out of 856 individuals; Supplementary material online, *Table S2*).

Since BrS is characterized by abnormal electrical activity in the right ventricle outflow track (RVOT) region, we compared Rad expression levels in mouse RVOT to its expression in the rest of the right ventricular and the left ventricular free walls. Rad was found four-fold more expressed in the RVOT than in the other ventricular parts (*Figure 2A*). We also investigated the expression of RAD in human left and right ventricles and observed higher expression in the subepicardium than in the subendocardium for both compartments (*Figure 2B*).

In order to decipher the electrophysiological consequences of the missense variant in *RRAD* (and/or possibly in *FHOD1*) within the family, we differentiated cardiomyocytes from iPSCs obtained from the index case (BrS1; individual III:2; three iPSC clones: BrS101, BrS102, and BrS103) and his unaffected brother (Ctl1; individual III:1; two clones: Ctl103 and Ctl104) who carries the rare variants on chromosomes 1 and 15 but not on chromosome 16.

Slow rate and reduced action potential upstroke velocity linked to I_{Na} and $I_{Ca,L}$ disruption in Brugada syndrome cardiomyocytes derived from induced pluripotent stem cells

We first investigated the properties of the ventricular-like action potentials. BrS1 iPSC-CMs displayed slower spontaneous rhythms than Ctl1 iPSC-CMs and lower action potential upstroke velocity (*Figure 3A–C*). Based on these results, we investigated the biophysical properties of the Na^+ and L-type Ca^{2+} currents. Membrane capacitance in BrS1 iPSC-CMs was slightly, though not significantly, higher (55.5 ± 25.5 pF, $n = 68$) than in Ctl1 iPSC-CMs (47.5 ± 22.8 pF; $n = 51$;

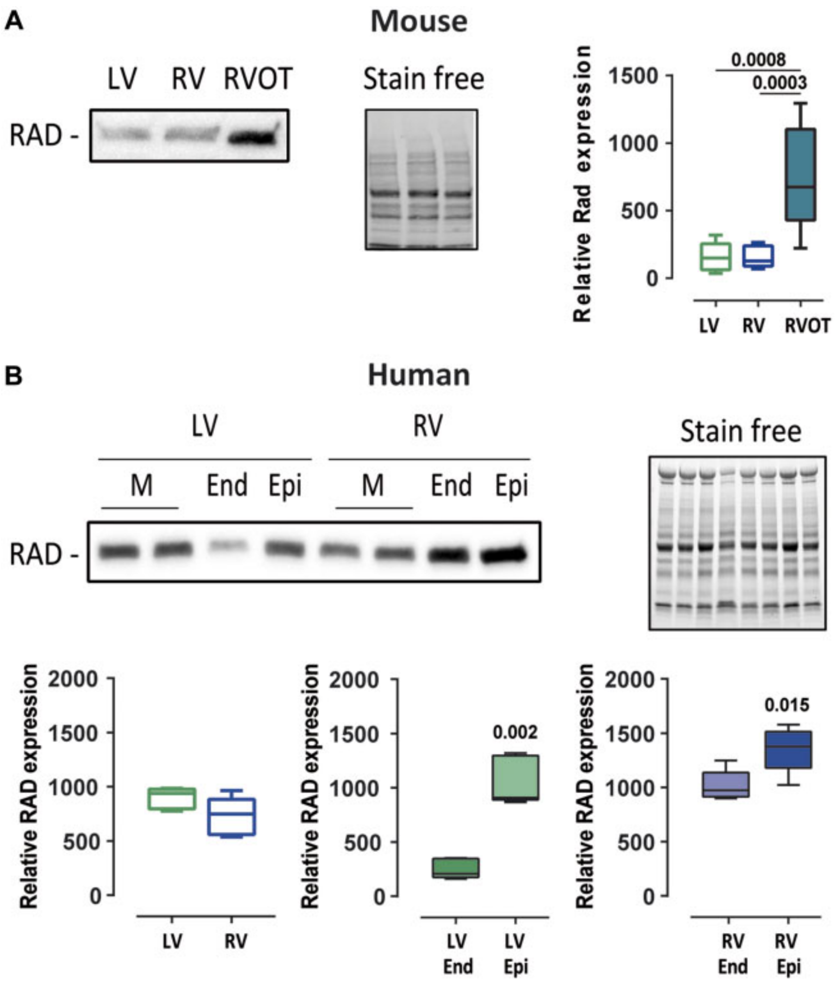

Figure 2 Rad protein expression pattern in mouse and human hearts. (*A*) Left: representative western blot of mouse Rad expression in the left ventricular free wall, the right ventricular free wall (without outflow tract), and the right ventricular outflow tract from one mouse. Right: box plot of Rad expression normalized to stain free for nine mice. Statistical test: Kruskal–Wallis test. (*B*) Top: representative western blot of RAD expression in left ventricular and right ventricular transmural (M), subendocardial (End), and subepicardial (Epi) samples from one individual. Bottom: box plots of RAD expression normalized to stain free for three individuals. Mann–Whitney test.

$P = 0.07$). I_{Na} density was significantly lower (by ~40% at -25 mV) in BrS1 iPSC-CMs (36.8 ± 16.7 pA/pF) than in Ctl1 iPSC-CMs (58.8 ± 16.5 pA/pF; *Figure* 3D *and E*), a result consistent with a lower $Na_V1.5$ protein level in BrS1 iPSC-CMs than in Ctl1 iPSC-CMs (Supplementary material online, *Figure S3*) while $Na_V1.5$ transcript level was not significantly changed (BrS1: 0.7 ± 0.4, 3 clones; Ctl1: 1.0 ± 0.5, 2 clones). Steady-state activation and inactivation gating properties did not differ between BrS1 and Ctl1 iPSC-CMs but recovery from inactivation was slightly faster in BrS1 iPSC-CMs than in Ctl1 iPSC-CMs (Supplementary material online, *Table S4*). I_{CaL} density was also lower (by ~30% at -5 mV) in BrS1 iPSC-CMs (18.9 ± 6.0 pA/pF) compared to Ctl1 iPSC-CMs (26.3 ± 7.1 pA/pF) without any disturbance of activation gating properties (*Figure 3F* and *G*; Supplementary material online, *Table S4*). Similar results have been obtained on iPSC-CMs derived from the proband's daughter carrying the p.R211H *RRAD* variant and affected by BrS (BrS2; individual IV:2; Supplementary material online, *Figure S4* and *Table S4*); her unaffected sister was used as control (Ctl2; individual IV:1). No difference in I_{Na} and I_{CaL} densities between the three BrS1 iPSC-CM clones and between the two Ctl1 iPSC-CM clones was observed (Supplementary material online, *Figure S5*).

Prolonged action potential duration, early afterdepolarizations, and calcium flux disturbances in Brugada syndrome cardiomyocytes derived from induced pluripotent stem cells

When paced at a cycle length of 700 ms, BrS1 iPSC-CMs showed longer action potentials than Ctl1 iPSC-CMs (*Figure 4A* and *B*). No significant difference was observed between the three BrS1 iPSC-CM clones and between the two Ctl1 iPSC-CM clones (Supplementary material online, *Figure S6*). Interestingly, BrS1

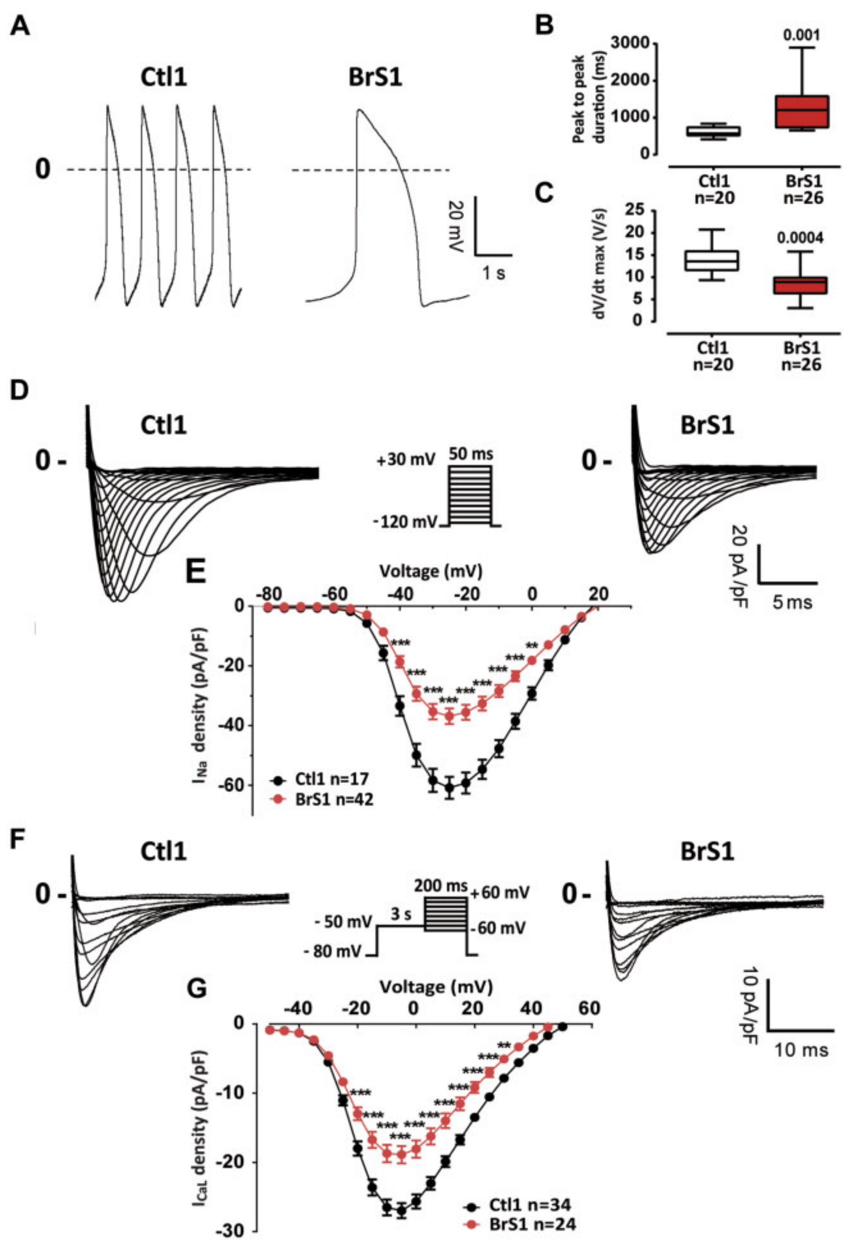

Figure 3 Spontaneous action potentials, I_{Na} and I_{CaL} properties in induced pluripotent stem cell-derived cardiomyocytes from the proband (BrS1) and his unaffected brother (Ctl1). (*A*) Representative action potential recordings of spontaneously beating Ctl1 and BrS1 cardiomyocytes derived from induced pluripotent stem cells. (*B* and *C*) Box plots of cycle length (*B*; spontaneous CL) and maximum upstroke velocity (*C*; dV/dT_{max}) of spontaneous action potentials. Statistical test: Mann–Whitney test. (*D* and *F*) Superimposed representative I_{Na} (*D*) and I_{CaL} (*F*) traces recorded in Ctl1 and BrS1 cardiomyocytes derived from induced pluripotent stem cells (voltage-clamp protocols in insets; stimulation frequency: 0.5 and 0.125 Hz for I_{Na} and I_{CaL}, respectively). (*E* and *G*) Mean (±SEM) current density-voltage relationship for peak I_{Na} (*E*) and $I_{Ca,L}$ (*G*). $^{**}P < 0.01$ and $^{***}P < 0.001$ (two-way analysis of variance with Bonferroni *post hoc* test for multiple comparisons).

iPSC-CMs also exhibited a larger persistent Na^+ current than Ctl1 iPSC-CMs *Figure 4C* and *D*). Early afterdepolarizations (EADs) were observed in 80% and 50% of BrS1 iPSC-CMs derived from BrS101 and BrS103 clones, respectively (*Figure 4E* and *F*) and in BrS2 iPSC-CMs (Supplementary material online, *Figure S4*). No EAD was observed in Ctl1 iPSC-CMs and in iPSC-CMs derived from clone BrS102.

Given these results, we investigated intracellular Ca^{2+} flux properties. BrS1 iPSC-CMs exhibited longer $[Ca^{2+}]_i$ transient decay times than Ctl1 iPSC-CMs (*Figure 4G* and *H*), suggesting an impairment of the Ca^{2+} recycling. Moreover, we observed abnormal $[Ca^{2+}]_i$ oscillations in 40% of the BrS1 iPSC-CMs (*Figure 4G*). These events are consistent with action potential prolongation and EAD appearance observed in these cells.

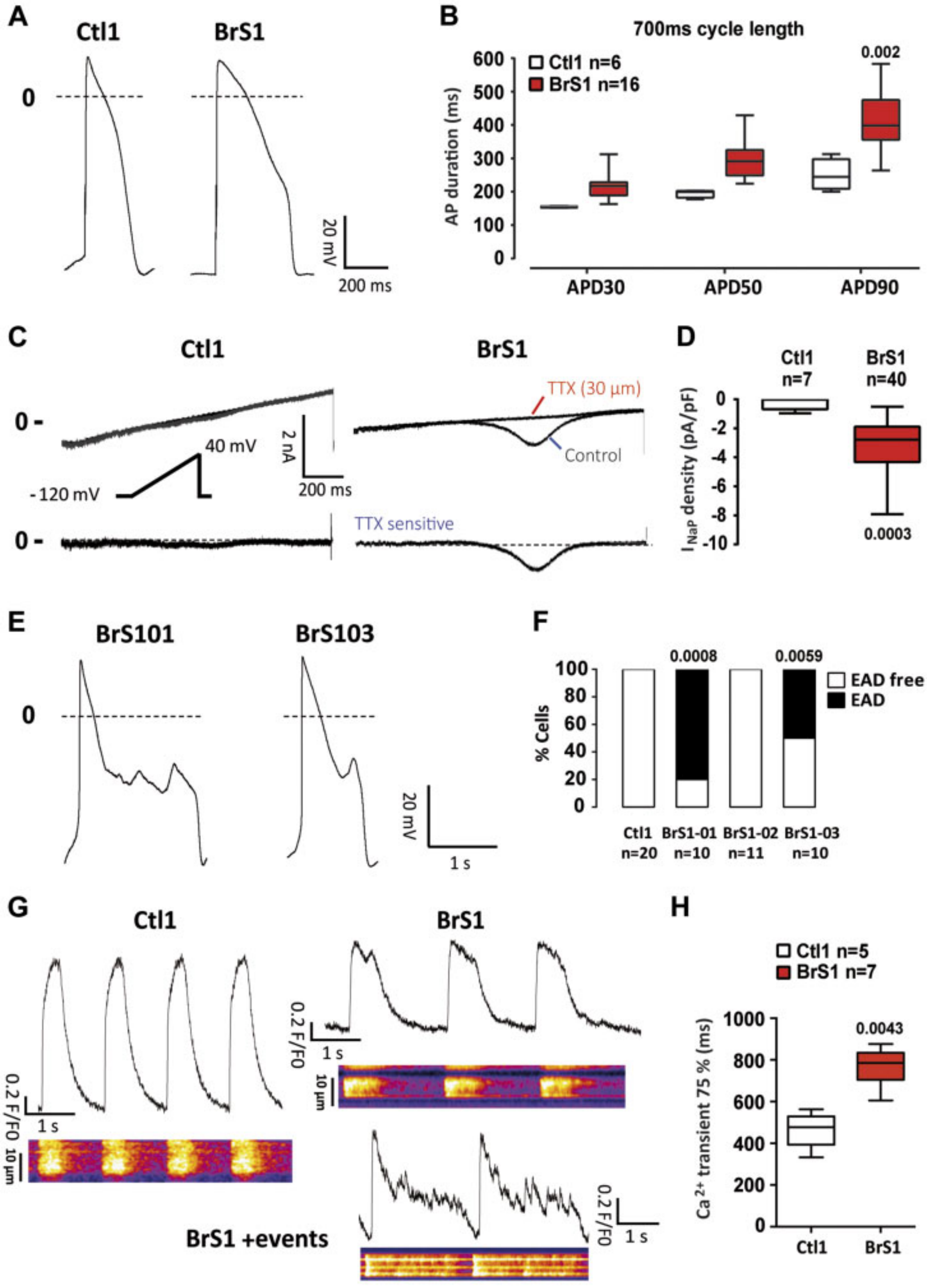

Figure 4 Action potential repolarization, persistent Na^+ current (I_{NaP}) and intracellular Ca^{2+} handling in cardiomyocytes derived from induced pluripotent stem cells from the proband (BrS1) and his unaffected brother (Ctl1). (*A*) Representative action potentials recorded at a pacing cycle length of 700 ms in Ctl1 and BrS1 cardiomyocytes derived from induced pluripotent stem cells. (*B*) Box plot of action potential duration (APD) at 30% (APD30), 50% (APD50), and 90% (APD90) of full repolarization. Statistical test: two-way analysis of variance with Bonferroni test for multiple comparisons. (*C*) Representative currents recorded during 1-s voltage-clamp ramps from -120 mV to +40 mV (inset; stimulation frequency: 0.2 Hz) before (Control) and after tetrodotoxin (TTX) perfusion (top traces) in Ctl1 and BrS1 cardiomyocytes derived from induced pluripotent stem cells Bottom traces show the corresponding TTX-sensitive currents. (*D*) Box plot of the TTX-sensitive I_{NaP} at -20 mV. Mann–Whitney test. (*E*) Representative examples of early afterdepolarizations recorded in spontaneously beating cardiomyocytes differentiated from BrS101 and BrS103 iPSC clones (BrS1 patient). (*F*) Early afterdepolarization incidence in the different cardiomyocytes derived from induced pluripotent stem cell lines. χ^2 test; *P* values vs. Ctl1. (*G*) Representative $[Ca^{2+}]_i$ transients from Ctl1 and BrS1 cardiomyocytes derived from induced pluripotent stem cells with an example of abnormal Ca^{2+} oscillations following peak $[Ca^{2+}]_i$ transient in BrS cardiomyocytes derived from induced pluripotent stem cells. (*H*) Box plot of $[Ca^{2+}]_i$ transient 75% decay time (Ca^{2+} transient 75%) in Ctl1 and BrS1 cardiomyocytes derived from induced pluripotent stem cells Mann–Whitney test.

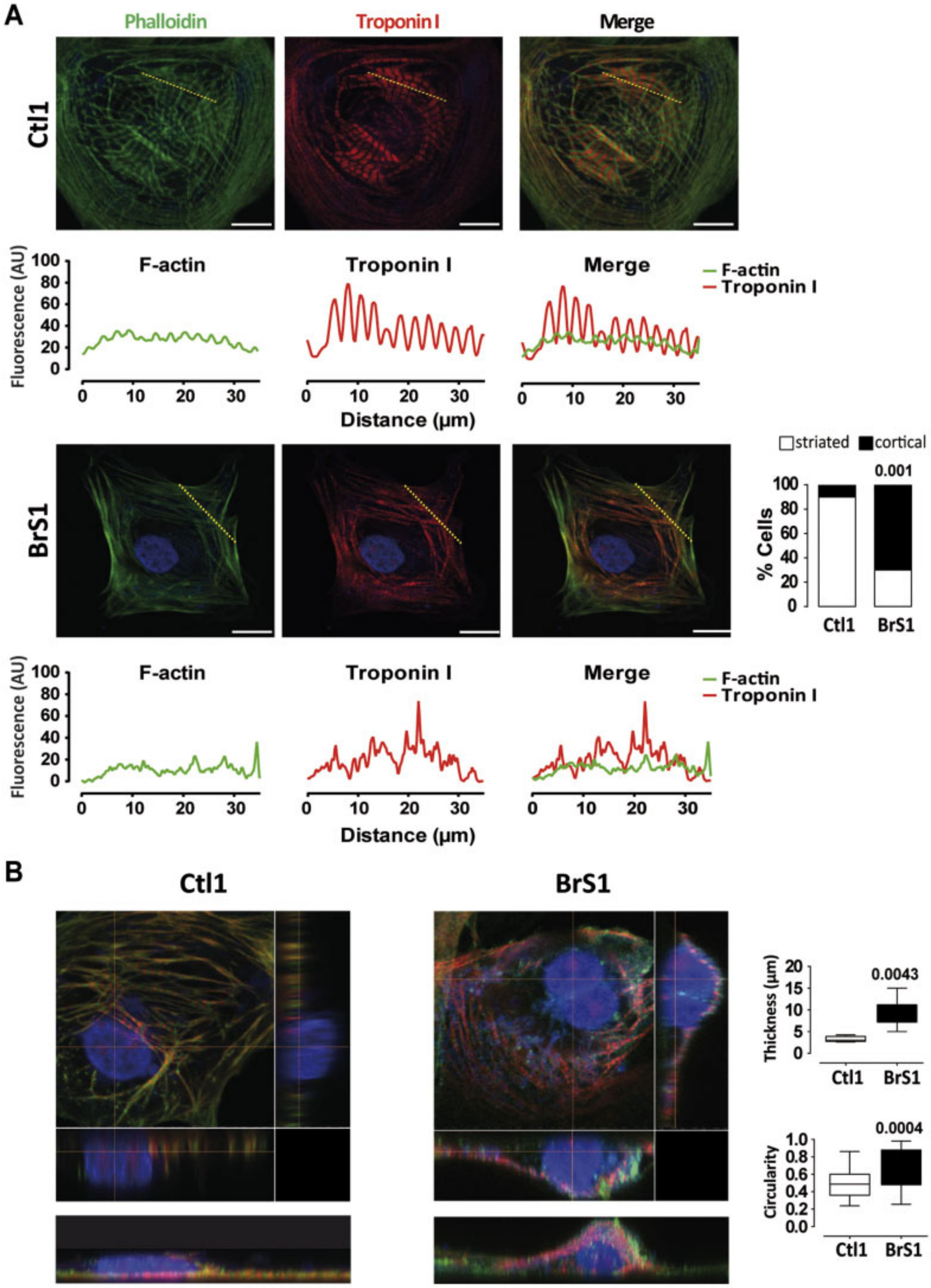

Figure 5 Cytoskeleton in cardiomyocytes derived from induced pluripotent stem cells obtained from the proband (BrS1) and his unaffected brother (Ctl1). (*A*) Left: representative immunostainings of filamentous actin (F-actin; stained with phalloidin) and troponin I and merged acquisitions with nucleus staining with DAPI in Ctl1 and BrS1 cardiomyocytes derived from induced pluripotent stem cells (top panels) and corresponding fluorescence distribution measured at the level of the yellow dotted lines (fluorescence-distance relationships; bottom panels). Scale bars: 20 µm. Right panel: percentage of Ctl1 (*n* = 10) and BrS1 (*n* = 18) cardiomyocytes derived from induced pluripotent stem cells with striated (in white) and cortical (in black) F-actin staining. Statistical test: Fisher's exact test. (*B*) Left: representative three-dimensional acquisition illustrations of a Ctl1 and a BrS1 cardiomyocytes derived from induced pluripotent stem cell after immunostaining of F-actin and Troponin I (left panels). Width: 107.12 µm; height: 12 µm; and depth: 107.12 µm. Right panel: box plots of thickness and cell circularity (cell width/cell length ratio) in Ctl1 (*n* = 10) and BrS1 (*n* = 12) cardiomyocytes derived from induced pluripotent stem cells Mann–Whitney test.

Cytoskeleton defects in Brugada syndrome cardiomyocytes derived from induced pluripotent stem cells

The BrS1 iPSC-CMs displayed impaired F-actin organization and cortical distribution of troponin I, while Ctl1 iPSC-CMs displayed a striated distribution of both proteins. This cytoskeleton defect was observed in 70% of BrS1 iPSC-CMs but in only 8% of Ctl1 iPSC-CMs (*Figure 5A*). Three-dimensional views using confocal microscopy showed that Ctl1 iPSC-CMs had flat cell bodies, whereas BrS1 iPSC-CMs exhibited round cell shape making the cell thickness larger than in Ctl1 iPSC-CMs (*Figure 5B*). In addition, the density of vinculin-containing adhesion complexes was lower in BrS1 iPSC-CMs than in Ctl1 iPSC-CMs, with impaired localization of vinculin (Supplementary material online, *Figure S7*). Similar results have been obtained in BrS2 iPSC-CMs (Supplementary material online, *Figure S8*).

RRAD p.R211H knock in isogenic line recapitulates the Brugada syndrome phenotype observed in the Brugada syndrome family members cell lines

RRAD p.R211H variant was inserted into an extra-familial control iPSC line by CRISPR/Cas9 technology (Supplementary material online, *Figure S9A*). Action potential recordings showed that genome edited (Rad R211H ins) iPSC-CMs had slower spontaneous rhythms, lower action potential upstroke velocity and longer action potential duration than control (Rad WT) iPSC-CMs (*Figure 6A–C*). Early afterdepolarizations were observed in 20% of Rad R211H ins iPSC-CMs and in none of the Rad WT iPSC-CMs (*Figure 6D*). Intracellular calcium recordings showed that Rad R211H ins iPSC-CMs exhibited uneven beating rate when compared with Rad WT iPSC-CMs as well as a slowing in the calcium reuptake (*Figure 6E* and *F*). Rad R211H ins iPSC-CMs exhibited a significantly lower peak I_{Na} density than Rad WT iPSC-CMs (30.3 ± 14.2 pA/pF vs. 56.8 ± 35.0 pA/pF, respectively, at -25 mV), with no change in steady-state activation and inactivation properties (Supplementary material online, *Table S4*). Rad R211H ins iPSC-CMs also exhibited a larger persistent Na^+ current than RAD WT iPSC-CMs (*Figure 6G* and *H*). No appreciable difference between Rad R211H ins iPSC-CMs and Rad WT iPSC-CMs in I_{CaL} density was observed (Supplementary material online, *Figure S9*). Finally, as in iPSC-CMs of the family members affected by BrS, the insertion of the p.R211H variant in the extra-familial control line triggered cytoskeleton defects in ∼40% of the cardiomyocytes (Supplementary material online, *Figure S9C*).

In addition, the effects of *RRAD* p.R211H variant were also investigated in neonatal mouse ventricular myocytes infected with adenoviruses encoding Green Fluorescent Protein (GFP) alone, wild type human RAD plus GFP, or p.R211H-RAD plus GFP. These experiments confirmed the results obtained with iPSC-CMs (Supplementary material online, *Results*).

The p.R211H variant triggers a gain of function effect on RAD GTPase activity

To directly assess the impact of the p.R211H variant on RAD activity, we performed nucleotide exchange kinetics measurements on WT-RAD and R211H-RAD proteins. As no guanine exchange factor is described for RAD GTPase, kinetics were initiated by Mg^{2+} chelation with ethylenediaminetetraacetic acid (EDTA) R211H-RAD protein showed an increased activity compared to WT-RAD (*Figure 7A* and *B*) with Kobs values that were significantly higher (respectively 0.083 ± 0.025 s^{-1} and 0.03 ± 0.008 s^{-1}). These results suggest that the variant has a direct positive effect on RAD GTPase activity, consistent with a gain of function of the protein.

Discussion

In this study, we identified a novel BrS-susceptibility gene, *RRAD*, and showed that the *RRAD* variant identified in a familial form of the disease leads to a BrS-typical electrical defect, i.e. reduced amplitude of I_{Na}, coupled with cardiomyocyte cytoskeletal abnormalities. At the cellular level, such dual effect has never been reported in the context of this hereditary arrhythmia.

In the past two decades, BrS has been associated to more than 20 susceptibility genes.[3,4] Most of those genes, including *SCN5A*, have been identified using functional candidate approaches, with only few mutations co-segregating with BrS ECG anomalies in familial forms. In the present study, we applied a hypothesis-free approach, based on whole-exome sequencing and identity-by-descent analysis, to a familial case with genetically unexplained BrS. Following this strategy, we identified six missense variants shared by the five family members exhibiting the BrS phenotype. Among these variants, the p.R211H substitution in the *RRAD* gene was (i) the least frequent in public databases (reported in only one case), (ii) the only variant predicted as deleterious by both SIFT and Polyphen-2, and (iii) the variant with the highest CADD score. These results indicate that p.R211H is the most likely causal variant in this familial case, independently of the biological function of *RRAD* gene product.

We then tested the relative contribution of *RRAD* variants in BrS susceptibility by screening for rare non-synonymous variants within its sequence among unrelated index cases compared to reference individuals, all of French origin. We observed a trend for enrichment in rare non-synonymous variants among cases ($P < 0.05$)—with 3/186 affected individuals carrying rare missense mutations vs. 2/856 reference individuals—thus strengthening the likelihood of *RRAD* involvement in BrS pathophysiology.

The RAD protein is a member of the RGK subfamily of Ras GTPases that has previously been associated with ventricular arrhythmias in mice.[14] Here, we showed higher levels of *RRAD* protein in subepicardium than in subendocardium in human heart, as well as predominant expression of Rad in the right ventricle outflow tract compared to the other cardiac compartments in mice: both expression patterns are fully concordant with a role in BrS pathogenesis.[6]

Results obtained with iPSC-CMs demonstrate that the *RRAD* p.R211H variant reduces I_{Na} by about 40%. To our knowledge, this is the first report of an effect of RAD on the cardiac Na^+ channel. The involvement of the *RRAD* p.R211H variant in I_{Na} down-regulation was confirmed by inserting the mutation by genome editing in a control human iPSC line obtained from a healthy individual unrelated to the family and by expressing the mutated protein in neonatal mouse ventricular cardiomyocytes in primary culture. The studies performed on this second model suggest that the p.R211H variant leads to a gain

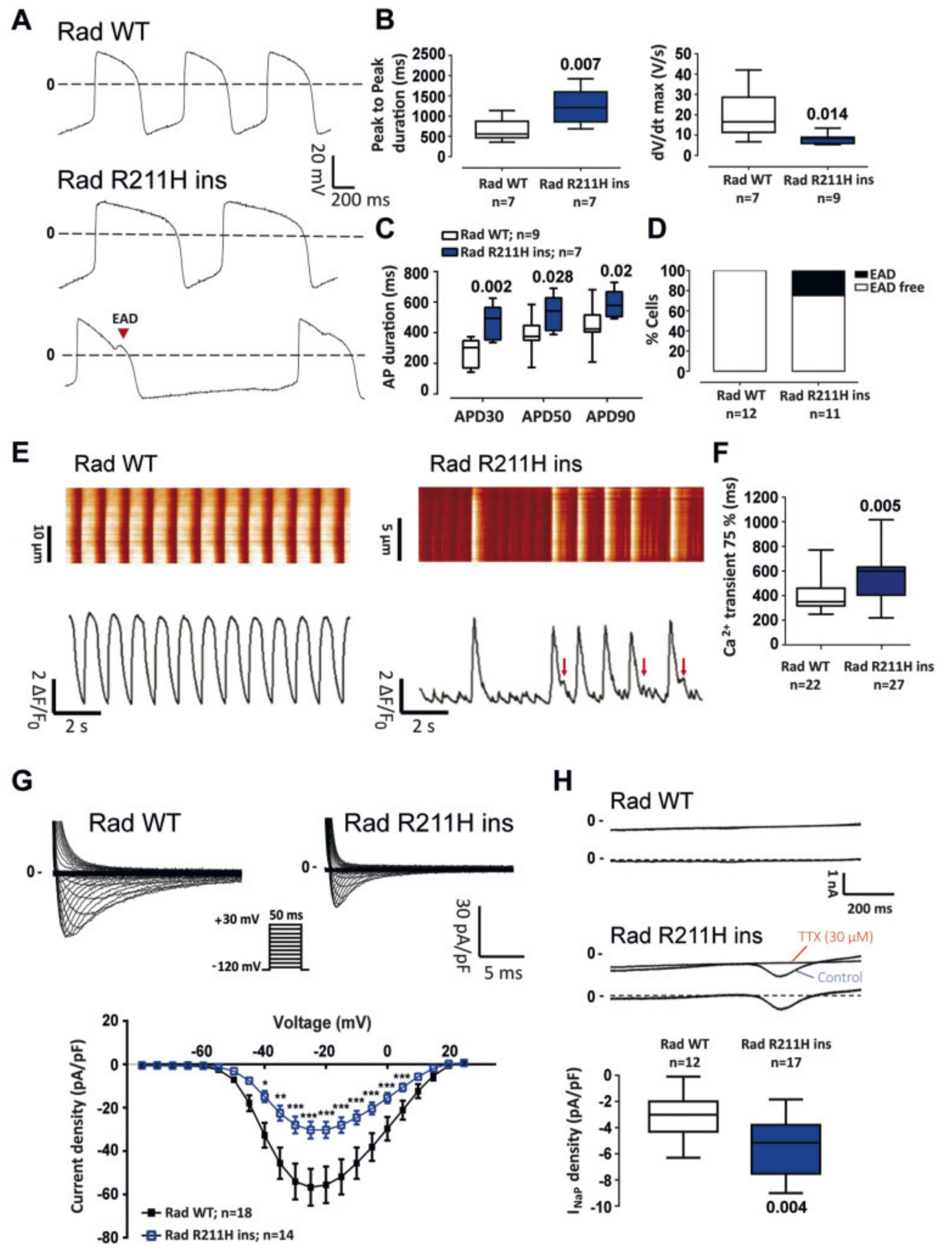

Figure 6 Rad p.R211H insertion in an extra-familial control line by genome editing: electrophysiological characterization. (*A*) Representative action potential recordings from control (Rad WT) and mutated (Rad WT) conditions. (*B*) Box plots of peak to peak duration and action potential upstroke velocity (*dV*/*dt* max) of Rad WT and Rad WT cardiomyocytes derived from induced pluripotent stem cells Mann–Whitney test. (*C*) Mean action potential duration (APD) at 30% (APD30), 50% (APD50), and 90% (APD90) of full repolarization at a pacing cycle length of 1 s. Two-way ANOVA with Bonferroni test for multiple comparisons. (*D*) Early afterdepolarization incidence in Rad WT and Rad R211H ins cardiomyocytes derived from induced pluripotent stem cells. (*E*) Representative $[Ca^{2+}]_i$ transients obtained in Rad WT and Rad R211H ins cardiomyocytes derived from induced pluripotent stem cells and their corresponding fluorescence map. (*F*) $[Ca^{2+}]_i$ transient 75% decay time (Ca^{2+} transient 75%) in Rad WT and Rad R211H ins cardiomyocytes derived from induced pluripotent stem cells Mann–Whitney test. (*G*) Superimposed representative I_{Na} traces recorded in Rad WT and Rad R211H ins cardiomyocytes derived from induced pluripotent stem cells (upper panel; voltage-clamp protocol in inset) and mean (±SEM) current density-membrane potential relationships (bottom). $^*P < 0.05$, $^{**}P < 0.01$, and $^{***}P < 0.001$ (two-way analysis of variance with Bonferroni *post hoc* test for multiple comparisons). (*H*) Top: representative currents recorded during 1-s voltage-clamp ramps from -120 mV to +40 mV (stimulation frequency: 0.2 Hz) before (Control) and after tetrodotoxin (TTX) perfusion (top traces) in Rad WT and Rad R211H ins cardiomyocytes derived from induced pluripotent stem cells and corresponding TTX-sensitive persistent sodium current (I_{NaP}, bottom traces). Bottom: box plots of I_{NaP} density. Mann–Whitney test.

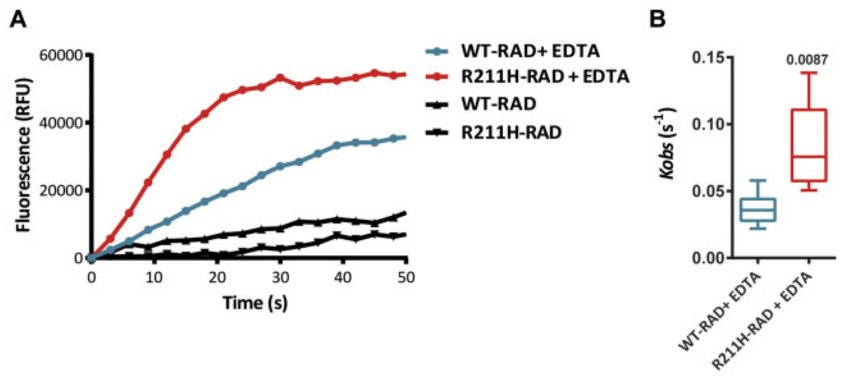

Figure 7 RAD protein GTPase activity analysis. (*A*) Representative fluorescence kinetics traces of WT-RAD and R211H-RAD GDP/GTP-mant exchange in the presence or absence of EDTA. (*B*) Box plot of K_{obs} values of EDTA-induced GDP/GTP-mant exchanges in WT-RAD ($n = 6$) and R211H-Rad ($n = 5$) cardiomyocytes. Statistical test: Mann–Whitney test.

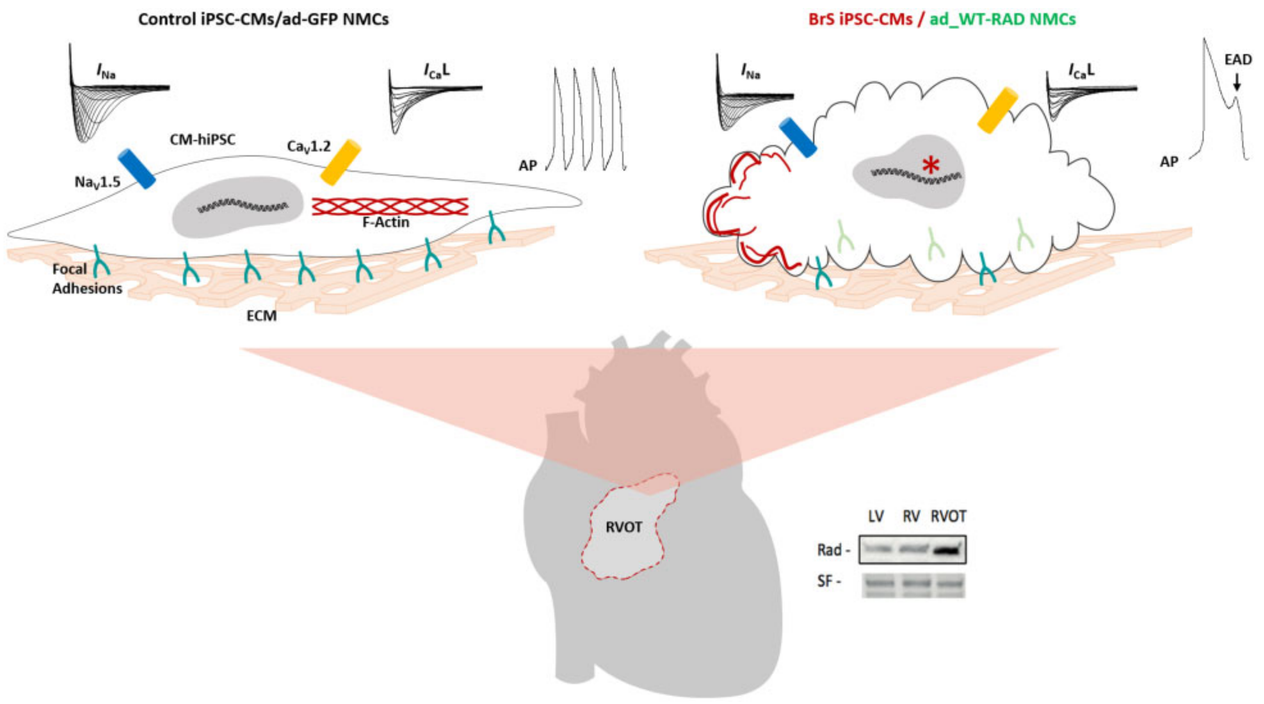

Take home figure The p.R211H mutation in the gene encoding RAD GTPase is involved in Brugada syndrome pathogenesis, leading to both electrical and structural defects in cardiomyocytes differentiated from induced pluripotent stem cells of affected patients.

of function of RAD. Indeed, its effect on I_{Na} is mimicked by a 10-fold overexpression of wild-type RAD and at this level of expression, both the WT and the p.R211H RAD have the same effect on I_{Na}. This gain-of-function hypothesis is supported by the two-fold faster GDP/GTP exchange activity of RAD that we found in the mutant protein compared to the WT RAD. Interestingly, the arginine-211 residue is highly conserved among species and among the RGK protein members. It is localized between the G4 and the G5 sites of the RAD guanine recognition area located in the G domain and may play an important role on RAD affinity for GTP.[15] Our results suggest that at least part of p.R211H RAD effects on I_{Na} involves a down-regulation of Nav1.5 expression at the protein level, without any alteration of *SCN5A* transcription. Further studies will be needed to elucidate the mechanisms of this down-regulation and whether RAD also interacts with Nav1.5 or one of its regulatory subunits to directly modulate its function.

The iPSC-CMs of the mutated patients and the genome edited Rad R211H ins iPSC-CMs were also characterized by the presence of a large persistent Na^+ current and the occurrence of EADs. The effects of *RRAD* p.R211H variant on the Na^+ current, i.e. a decrease in Na^+ peak current amplitude and the occurrence of a persistent Na^+ current, are similar to those produced by the *SCN5A* mutation p.1795insD, which causes an overlap syndrome combining the phenotypic traits of BrS and Type 3 long QT syndrome.[16] However, mouse studies suggest that RAD is preferentially expressed in the RVOT which could limit the effects of the mutation to this specific area, which is insufficient to trigger appreciable QT prolongation. This would explain why the *RRAD* p.R211H carriers exhibit normal QT intervals.

At first glance, EADs are not expected to be involved in arrhythmias in the context of BrS. However, they have also been observed in iPSC-CMs from a BrS patient with a *TBX5* gene variant,[17] as well as in iPSC-CMs of BrS patients carrying *SCN5A* mutations.[18] In this latter study, those arrhythmic events were linked to abnormal Ca^{2+} handling, which also led to delayed afterdepolarizations. The investigation of Ca^{2+} handling in our BrS1 and Rad R211H ins cell lines showed delayed Ca^{2+} recapture and abnormal Ca^{2+} release during recapture in both lines. Combined with the persistent Na^+ current, these results are consistent with the APD prolongation and EAD appearance. This phenomenon could be linked to the immaturity of the cells: on the one hand, a recent study showed that until day 30 of differentiation, iPS-CMs express a different isoform of $Na_V1.5$ protein,[19] and on the other hand $Ca_V1.2$ is not properly localized close to the ryanodine receptor RYR2 due to the absence of T-tubule structures.[20] These phenotypic traits seem to be characteristic of BrS in iPSC-CMs but their involvement in triggering arrhythmias in the patient remains uncertain.

The iPSC-CMs of the family members carrying the *RRAD* p.R211H variant were also characterized by a reduction of the L-type Ca^{2+} current compared to intra-familial control iPSC-CMs. A reduction of this current has already been involved in some forms of BrS.[6,21] Interestingly, RAD has previously been shown to regulate the cardiac L-type Ca^{2+} current by controlling the Cav1.2 channel trafficking to the sarcolemma.[14,22] Altogether, these data suggested that the pathophysiological mechanisms of *RRAD*-related BrS included a combined decrease of both Na^+ and Ca^{2+} current amplitude, which had never been described before. However, the investigation of the isogenic Rad R211H ins iPSC-CMs only confirmed the loss of function of the Na^+ current. This discrepancy could be explained by the presence of other variant(s) limiting this dual electrical modulation to this particular family. Nonetheless, the isogenic model validates that *RRAD* p.R211H variant is sufficient to provoke a pro-arrhythmic phenotype and suggests that the main BrS causal defects induced by this variant are a dysregulation of the Na^+ channel and an alteration of the cytoskeleton.

Indeed, in addition to the electrical defects, *RRAD* p.R211H disorganizes the striated architecture of the cardiomyocyte cytoskeleton, and disturbs the localization of focal adhesions, which leads to cell rounding. Again here, the gain-of-function effect of the mutation RAD GTPase activity is proven, since the overexpression of WT RAD induces similar effects in neonatal mouse cardiomyocytes, and more severely with the overexpression of p.R211H-RAD. RAD is known to interact with the cytoskeleton.[23,24] In the present study, RAD p.R211H acts like a down-regulator of the F-actin cytoskeleton consolidation - most likely through the inhibition of Rho Kinase activity (Supplementary material online, *Figure S12*), leading to a decrease in cell contractility and focal adhesion formation and maturation.[25] These structural defects, which might be limited to the RVOT given the preferred localization of RAD protein in this cardiac region, could lead to decreased cell-to-cell connection and abnormal cardiac conduction[26] and thus play a role in BrS. There are indeed accumulating evidences that structural anomalies in the myocardium, such as fatty infiltrations and fibrosis, may trigger electrical anomalies in relation to BrS.[27–29] Furthermore, several susceptibility genes or loci, such as *MOG1*[30,31] or *HEY2*, have been shown to regulate not only electrical activity but also cardiac morphogenesis.[32,33] Taken together, these data indicate that structural ventricular anomalies may contribute significantly to the expression of the electrical features typical of BrS.

Study limitations

One of the limitations of the present study relates to the immature state of the iPSC-CMs. At the electrical level, the lack of I_{K1} and the low I_{to} density prevent the cardiomyocytes to display proper action potential shape and resting membrane potential. At the structural level, the absence of cell polarity and T-tubule structures makes it difficult to study calcium handling and cytoskeleton integrity due to lack of proper localization of the proteins involved. Moreover, Brugada syndrome being related to RVOT, these cells fail to capture the complexity of the phenotype due to lack of cardiac layer specification (endocardium, myocardium, and epicardium) and chamber specification (right or left ventricles/auricles). Despite these limitations, the fact that iPSC-CMs express the main ion currents and display spontaneous contractile activity makes it an accurate model to study the impact of a specific variant at the single cell level in a patient-specific manner.

In conclusion, p.R211H *RRAD* variant induces a gain of function of RAD, which reduces the amplitude of the Na^+ current, a mechanism already associated with BrS, and induces a persistent Na^+ current. In addition, this variant leads to cytoskeleton anomalies and defects in cell morphology. This impaired structural integrity of cardiomyocytes, which had never been related to BrS, might alter conduction by destabilizing myocardial structure. Furthermore, the fact that the insertion of the mutation in an external control cell line recapitulates the overall phenotype confirms the involvement of the p.R211H *RRAD* variant in the BrS phenotype observed in the other models. The relative contribution of myocardial structural abnormalities vs. electrical alterations remains uncertain and should be subjected to further investigations.

Supplementary material

Supplementary material is available at *European Heart Journal* online.

Acknowledgements

The authors thank Virginie Forest and Agnès Carcouet (*l'institut du thorax*) for their expert technical assistance, as well as the members of the *Centre d'Investigation Clinique* and the *Centre de Référence des troubles du rythme héréditaires ou rares de l'Ouest* and the *Centre de Ressources Biologiques* at the CHU of Nantes. Genomic analysis, confocal imaging experiments, and neonatal mouse cardiomyocyte isolation and culture were performed with the support of the *GenoBIRD*, *MicroPiCell*, and *Therassay* core facilities (Biogenouest), respectively. Finally, the authors are grateful to the patients and families who agreed to participate in the research.

Funding

This work was supported by the *Fondation pour la Recherche Médicale* (*Equipe FRM* DEQ20140329545 to J.J.S.), the *Agence Nationale de la Recherche* (ANR-12-BSC1-0013-01 to F.C., ANR-14-CE10-0001-01 to R.R., ANR-15-CE14-0019-01 to N.G., ANR-15-CE14-0006-01 to C.M.), the National Institutes of Health (R01 HL128170 to J.C.W.), the Leducq Foundation (18CVD05 to J.C.W.), the *Fédération Française de Cardiologie* (FFC R15070NN to N.G.; *subvention FFC 2017* to V.P.), and the Pays-de-la-Loire regional council (VaCaRMe programme to R.R.).

Conflict of interest: J.C.W. is a co-founder of Khloris Biosciences. All other authors have nothing to disclose.

References

1. Brugada P, Brugada J. Right bundle branch block, persistent ST segment elevation and sudden cardiac death: a distinct clinical and electrocardiographic syndrome. A multicenter report. *J Am Coll Cardiol* 1992;**20**:1391–1396.
2. Priori SG, Blomström-Lundqvist C, Mazzanti A, Blom N, Borggrefe M, Camm J, Elliott PM, Fitzsimons D, Hatala R, Hindricks G, Kirchhof P, Kjeldsen K, Kuck KH, Hernandez-Madrid A, Nikolaou N, Norekvål TM, Spaulding C, Van Veldhuisen DJ; ESC Scientific Document Group. 2015 ESC Guidelines for the management of patients with ventricular arrhythmias and the prevention of sudden cardiac death: the Task Force for the Management of Patients with Ventricular Arrhythmias and the Prevention of Sudden Cardiac Death of the European Society of Cardiology (ESC). Endorsed by: association for European Paediatric and Congenital Cardiology (AEPC). *Eur Heart J* 2015;**36**:2793–2867.
3. Kapplinger JD, Tester DJ, Alders M, Benito B, Berthet M, Brugada J, Brugada P, Fressart V, Guerchicoff A, Harris-Kerr C, Kamakura S, Kyndt F, Koopmann TT, Miyamoto Y, Pfeiffer R, Pollevick GD, Probst V, Zumhagen S, Vatta M, Towbin JA, Shimizu W, Schulze-Bahr E, Antzelevitch C, Salisbury BA, Guicheney P, Wilde AA, Brugada R, Schott JJ, Ackerman MJ. An international compendium of mutations in the SCN5A-encoded cardiac sodium channel in patients referred for Brugada syndrome genetic testing. *Heart Rhythm* 2010;**7**:33–46.
4. Andorin A, Behr ER, Denjoy I, Crotti L, Dagradi F, Jesel L, Sacher F, Petit B, Mabo P, Maltret A, Wong LC, Degand B, Bertaux G, Maury P, Dulac Y, Delasalle B, Gourraud JB, Babuty D, Blom NA, Schwartz PJ, Wilde AA, Probst V. Impact of clinical and genetic findings on the management of young patients with Brugada syndrome. *Heart Rhythm* 2016;**13**:1274–1282.
5. Postema PG, van Dessel PF, Kors JA, Linnenbank AC, van Herpen G, Ritsema van Eck HJ, van Geloven N, de Bakker JM, Wilde AA, Tan HL. Local depolarization abnormalities are the dominant pathophysiologic mechanism for type 1 electrocardiogram in Brugada syndrome. A study of electrocardiograms, vectorcardiograms, and body surface potential maps during ajmaline provocation. *J Am Coll Cardiol* 2010;**55**:789–797.
6. Gourraud J-B, Barc J, Thollet A, Le Scouarnec S, Le Marec H, Schott JJ, Redon R, Probst V. The Brugada syndrome: a rare arrhythmia disorder with complex inheritance. *Front Cardiovasc Med* 2016;**3**:1–11.
7. Portero V, Le Scouarnec S, Es-Salah-Lamoureux Z, Burel S, Gourraud JB, Bonnaud S, Lindenbaum P, Simonet F, Violleau J, Baron E, Moreau E, Scott C, Chatel S, Loussouarn G, O'Hara T, Mabo P, Dina C, Le Marec H, Schott JJ, Probst V, Baró I, Marionneau C, Charpentier F, Redon R. Dysfunction of the voltage-gated K$^+$ channel β_2 subunit in a familial case of Brugada syndrome. *J Am Heart Assoc* 2016;**5**:e003122.
8. Risgaard B, Jabbari R, Refsgaard L, Holst AG, Haunsø S, Sadjadieh A, Winkel BG, Olesen MS, Tfelt-Hansen J. High prevalence of genetic variants previously associated with Brugada syndrome in new exome data. *Clin Genet* 2013;**84**:489–495.
9. Le Scouarnec S, Karakachoff M, Gourraud JB, Lindenbaum P, Bonnaud S, Portero V, Duboscq-Bidot L, Daumy X, Simonet F, Teusan R, Baron E, Violleau J, Persyn E, Bellanger L, Barc J, Chatel S, Martins R, Mabo P, Sacher F, Haïssaguerre M, Kyndt F, Schmitt S, Bézieau S, Le Marec H, Dina C, Schott JJ, Probst V, Redon R. Testing the burden of rare variation in arrhythmia-susceptibility genes provides new insights into molecular diagnosis for Brugada syndrome. *Hum Mol Genet* 2015;**24**:2757–2763.
10. Ackerman MJ. Genetic purgatory and the cardiac channelopathies: exposing the variants of uncertain/unknown significance issue. *Heart Rhythm* 2015;**12**: 2325–2331.
11. Probst V, Wilde AAM, Barc J, Sacher F, Babuty D, Mabo P, Mansourati J, Le Scouarnec S, Kyndt F, Le Caignec C, Guicheney P, Gouas L, Albuisson J, Meregalli PG, Le Marec H, Tan HL, Schott JJ. SCN5A mutations and the role of genetic background in the pathophysiology of Brugada syndrome. *Circ Cardiovasc Genet* 2009;**2**:552–557.
12. Bezzina CR, Barc J, Mizusawa Y, Remme CA, Gourraud JB, Simonet F, Verkerk AO, Schwartz PJ, Crotti L, Dagradi F, Guicheney P, Fressart V, Leenhardt A, Antzelevitch C, Bartkowiak S, Borggrefe M, Schimpf R, Schulze-Bahr E, Zumhagen S, Behr ER, Bastiaenen R, Tfelt-Hansen J, Olesen MS, Kääb S, Beckmann BM, Weeke P, Watanabe H, Endo N, Minamino T, Horie M, Ohno S, Hasegawa K, Makita N, Nogami A, Shimizu W, Aiba T, Froguel P, Balkau B, Lantieri O, Torchio M, Wiese C, Weber D, Wolswinkel R, Coronel R, Boukens BJ, Bézieau S, Charpentier E, Chatel S, Despres A, Gros F, Kyndt F, Lecointe S, Lindenbaum P, Portero V, Violleau J, Gessler M, Tan HL, Roden DM, Christoffels VM, Le Marec H, Wilde AA, Probst V, Schott JJ, Dina C, Redon R. Common variants at SCN5A-SCN10A and HEY2 are associated with Brugada syndrome, a rare disease with high risk of sudden cardiac death. *Nat Genet* 2013;**45**: 1044–1049.
13. Reynet C, Kahn CR. Rad: a member of the Ras family overexpressed in muscle of type II diabetic humans. *Science* 1993;**262**:1441–1444.
14. Yada H, Murata M, Shimoda K, Yuasa S, Kawaguchi H, Ieda M, Adachi T, Murata M, Ogawa S, Fukuda K. Dominant negative suppression of Rad leads to QT prolongation and causes ventricular arrhythmias via modulation of L-type Ca^{2+} channels in the heart. *Circ Res* 2007;**101**:69–77.
15. Rojas AM, Fuentes G, Rausell A, Valencia A. The Ras protein superfamily: evolutionary tree and role of conserved amino acids. *J Cell Biol* 2012;**196**:189–201.
16. Portero V, Casini S, Hoekstra M, Verkerk AO, Mengarelli I, Belardinelli L, Rajamani S, Wilde AAM, Bezzina CR, Veldkamp MW, Remme CA. Anti-arrhythmic potential of the late sodium current inhibitor GS-458967 in murine Scn5a-1798insD+/- and human SCN5A-1795insD+/- iPSC-derived cardiomyocytes. *Cardiovasc Res* 2017;**113**:829–838.
17. Bersell KR, Yang T, Hong CC, Wells QS, Kannankeril PJ, Roden DM. Genomic editing in iPSCs establishes that a rare TBX5 variant causes Brugada syndrome. *Heart Rhythm* 2016;**13**(Suppl):S9.
18. Liang P, Sallam K, Wu H, Li Y, Itzhaki I, Garg P, Zhang Y, Vermglinchan V, Lan F, Gu M, Gong T, Zhuge Y, He C, Ebert AD, Sanchez-Freire V, Churko J, Hu S, Sharma A, Lam CK, Scheinman MM, Bers DM, Wu JC. Patient-specific and genome-edited induced pluripotent stem cell-derived cardiomyocytes elucidate single cell phenotype of Brugada syndrome. *J Am Coll Cardiol* 2016;**68**:2086–2096.
19. Veerman CC, Mengarelli I, Lodder EM, Kosmidis G, Bellin M, Zhang M, Dittmann S, Guan K, Wilde AAM, Schulze-Bahr E, Greber B, Bezzina CR, Verkerk AO. Switch from fetal to adult SCN5A isoform in human induced pluripotent stem cell-derived cardiomyocytes unmasks the cellular phenotype of a conduction disease-causing mutation. *J Am Heart Assoc* 2017;**6**:e005135.
20. Satin J, Itzhaki I, Rapoport S, Schroder EA, Izu L, Arbel G, Beyar R, Balke CW, Schiller J, Gepstein L. Calcium handling in human embryonic stem cell-derived cardiomyocytes. *Stem Cells* 2008;**26**:1961.
21. Antzelevitch C, Pollevick GD, Cordeiro JM, Casis O, Sanguinetti MC, Aizawa Y, Guerchicoff A, Pfeiffer R, Oliva A, Wollnik B, Gelber P, Bonaros EP Jr, Burashnikov E, Wu Y, Sargent JD, Schickel S, Oberheiden R, Bhatia A, Hsu LF, Haïssaguerre M, Schimpf R, Borggrefe M, Wolpert C. Loss-of-function mutations in the cardiac calcium channel underlie a new clinical entity characterized by ST-segment elevation, short QT intervals, and sudden cardiac death. *Circulation* 2007;**115**:442–449.
22. Wang G, Zhu X, Xie W, Han P, Li K, Sun Z, Wang Y, Chen C, Song R, Cao C, Zhang J, Wu C, Liu J, Cheng H. Rad as a novel regulator of excitation-contraction coupling and β-adrenergic signaling in heart. *Circ Res* 2010;**106**: 317–327.
23. Zhu J, Bilan PJ, Moyers JS, Antonetti DA, Kahn CR. Rad, a novel Ras-related GTPase, interacts with skeletal muscle beta-tropomyosin. *J Biol Chem* 1996;**271**: 768–773.
24. Bilan PJ, Moyers JS, Kahn CR. The Ras-related protein rad associates with the cytoskeleton in a non-lipid-dependent manner. *Exp Cell Res* 1998;**242**:391–400.
25. Ward Y, Yap SF, Ravichandran V, Matsumura F, Ito M, Spinelli B, Kelly K. The GTP binding proteins Gem and Rad are negative regulators of the Rho-Rho kinase pathway. *J Cell Biol* 2002;**157**:291–302.
26. Kant S, Holthöfer B, Magin TM, Krusche CA, Leube RE. Desmoglein 2-dependent arrhythmogenic cardiomyopathy is caused by a loss of adhesive function. *Circ Cardiovasc Genet* 2015;**8**:553–563.
27. Catalano O, Antonaci S, Moro G, Mussida M, Frascaroli M, Baldi M, Cobelli F, Baiardi P, Nastoli J, Bloise R, Monteforte N, Napolitano C, Priori SG. Magnetic resonance investigations in Brugada syndrome reveal unexpectedly high rate of structural abnormalities. *Eur Heart J* 2009;**30**:2241–2248.

28. Nademanee K, Raju H, de Noronha SV, Papadakis M, Robinson L, Rothery S, Makita N, Kowase S, Boonmee N, Vitayakritsirikul V, Ratanarapee S, Sharma S, van der Wal AC, Christiansen M, Tan HL, Wilde AA, Nogami A, Sheppard MN, Veerakul G, Behr E. Fibrosis, connexin-43, and conduction abnormalities in the Brugada syndrome. *J Am Coll Cardiol* 2015;**66**:1976–1986.
29. Sieira J, Dendramis G, Brugada P. Pathogenesis and management of Brugada syndrome. *Nat Rev Cardiol* 2016;**13**:744–756.
30. Kattygnarath D, Maugenre S, Neyroud N, Balse E, Ichai C, Denjoy I, Dilanian G, Martins RP, Fressart V, Berthet M, Schott JJ, Leenhardt A, Probst V, Le Marec H, Hainque B, Coulombe A, Hatem SN, Guicheney P. MOG1: a new susceptibility gene for Brugada syndrome. *Circ Cardiovasc Genet* 2011;**4**:261–268.
31. Zhou J, Wang L, Zuo M, Wang X, Ahmed AS, Chen Q, Wang QK. Cardiac sodium channel regulator MOG1 regulates cardiac morphogenesis and rhythm. *Sci Rep* 2016;**6**:21538.
32. Sakata Y, Kamei CN, Nakagami H, Bronson R, Liao JK, Chin MT. Ventricular septal defect and cardiomyopathy in mice lacking the transcription factor CHF1/Hey2. *Proc Natl Acad Sci USA* 2002;**99**:16197–16202.
33. Veerman CC, Podliesna S, Tadros R, Lodder EM, Mengarelli I, de Jonge B, Beekman L, Barc J, Wilders R, Wilde AAM, Boukens BJ, Coronel R, Verkerk AO, Remme CA, Bezzina CR. The Brugada syndrome susceptibility gene HEY2 modulates cardiac transmural ion channel patterning and electrical heterogeneity. *Circ Res* 2017;**121**:537–548.

RRAD mutation causes electrical and cytoskeletal defects in cardiomyocytes derived from a familial case of Brugada syndrome

ONLINE DATA SUPPLEMENT

Online supplementary methods

The study was conducted according to the principles set forth under the Declaration of Helsinki (1989) and European guidelines for clinical and genetic research. Institutional review board approvals of the study were obtained before the initiation of patient enrolment. Informed written consent was obtained from each patient who agreed to participate in the clinical and genetic study.

H9 human embryonic stem cells were used as positive controls for human induced pluripotent stem cell characterization under agreement n°RE13-004 from the *Agence de la Biomédecine.*

Clinical recruitment

The diagnosis of Brugada syndrome (BrS) was based on the presence of a typical type 1 ECG pattern, either spontaneous or pharmacologically-induced, in at least one right precordial lead (V1, V2, V3) in the 3rd or 4th intercostal space, according to 2013 recommendations (1). Two physicians blinded to the clinical and genetic status reviewed ECGs recorded before and during flecainide challenge. Measurements were performed using Image J software (National Institutes of Health, Bethesda, Maryland; http://rsb. info.nih.gov/ij) as previously described (2). Clinical follow-up was collected prospectively from either the referring cardiologists or directly from the patients.

Exome sequencing, identity-by-descent (IBD) analysis and rare variant filtering

Exome sequencing was performed on the proband of a French family with 5 affected individuals. After Agilent SureSelect capture (3) sequencing was carried out on Illumina Genome Analyzer IIx to a mean depth of 87x, as previously described (4). Reads were aligned to the human genome assembly GRCh37 with BWA-MEM (version 0.7.6a). Genetic variations (single nucleotide variants and indels) were called using Samtools v0.1.19, GATK Unified Genotyper and GATK Haplotype Caller v2.8 and were considered for further analyses if detected by at least two calling algorithms. Functional consequences were annotated using Variant Effect Predictor (5), with Ensembl release 75. Variants with the following consequences were selected: ñtranscript_ablationò (SO:0001893), ñsplice_donor_variantò (SO:0001575), ñsplice_acceptor_variantò (SO:0001574), ñstop_gainedò (SO:0001587), ñframeshift_variantò (SO:0001589), ñstop_lostò (SO:0001578), ñstart_lostò (SO:0002012), òprotein_altering_variant" (SO:0001818) ñinframe_insertionò (SO:0001821), ñinframe_deletionò (SO:0001822), ñmissense_variantò (SO:0001583), ñtranscript_amplificationò (SO:0001889). Variants with a minor allele frequency < 0.1% in all ExAC populations (Exome Aggregation Consortium, http://exac.broadinstitute.org/, version 0.3, 60,706 individuals) (6) were considered as rare. Subsequently, allele frequencies from the gnomAD database were interrogated (genome Aggregation Database, http://gnomad.broadinstitute.org/, 138,632 individuals). The potential deleteriousness of missense variants was assessed with SIFT (7), PolyPhen-2 (8) and CADD (9). Knime4Bio, a set of custom nodes for the interpretation of next-generation sequencing data with KNIME (10) was used for all filtering steps. To determine regions shared by all affected individuals (IBD, identity-by-descent), SNP genotyping was performed on population-optimized Affymetrix Axiom Genome-Wide CEU 1 array plates following the standard manufacturer's protocol. Fluorescence intensities were quantified using the Affymetrix GeneTitan Multi-Channel Instrument, and primary analysis was conducted with Affymetrix Power Tools following the manufacturer's recommendations. All individuals had a genotype call rate above 97%. SNPs with a minor allele frequency (MAF) < 10%, a genotyping rate < 95% or with $P < 1 \times 10^{-5}$ when testing for Hardy-Weinberg equilibrium were excluded.

IBD estimation was performed with IBDLD v3.34 using the NoLD option (11). Shared regions were obtained by analysing two sets of independent SNPs ($r^2 < 0.2$) using the PREGO cohort as a reference panel. Finally, all rare variants with potential functional consequence located in IBD regions were confirmed and tested for co-segregation by Sanger sequencing. Sanger sequencing was carried out on an Applied Biosystems 3730 DNA Analyzer, using standard procedures. In order to test enrichment in the proportion of individuals carrying rare non-synonymous variants in *RRAD* among 186 index cases with BrS, the Cohort Allelic Sums Test (CAST, based on a Fisher's test) was applied (12). This test consists in comparing the proportion of cases and controls carrying at least one variant. The control set comprised 856 individuals originating from western France, for whom the *RRAD* status was extracted from whole-genome sequencing at a mean read depth of 37X. Only non-synonymous variants and canonical splice sites with an allele frequency lower than 0.1% in the Non-Finnish European population from the gnomAD whole-genome sequencing dataset were considered as rare and included in the test (based on RefSeq transcript NM_004165.3).

Generation and characterization of human induced pluripotent stem cell (iPSC) lines

Generation of iPSC. The iPSC lines from the proband (individual III:2; 3 lines: BrS101, BrS102, BrS103), his unaffected brother (III:1) who did not carry the *RRAD* variant (2 lines: Ctl103, Ctl104), his affected daughter (IV:2; 1 line) and his unaffected daughter (IV:1; 1 line) were generated from peripheral blood mononuclear cells (PBMCs) in the iPSC core facility of Nantes University. PBMCs were reprogrammed by Sendai viruses expressing Oct4, Sox2, Klf4 and c-Myc (CytoTune^{TM}-IPS 2.0 Sendai Reprogramming kit, Life Technologies). The iPSC clones were picked and expanded on mouse embryonic fibroblasts (MEFs) feeder cells in KSR-FGF2 medium (DMEM/F12 supplemented with 0.1% β-mercaptoethanol, 20% knockout serum replacement, 10 ng/mL basic fibroblast growth factor, 2 mmol/L l-glutamine and 1% NEAA). Until P10, colonies were mechanically passaged with a needle. At P10, iPSC clones were adapted to feeder-free culture conditions: stem cell-qualified Matrigel-coated plates (0.1 mg/mL; BD Bioscience) with IPs Brew XF medium (StemMACS^{TM}, Miltenyi Biotec). Feeder-free iPSCs were passaged using the Passaging Solution XF (StemMACS^{TM}, Miltenyi Biotec).

Pluripotency confirmation. The expression of pluripotency markers in the generated cell lines was verified by RT-PCR for OCT4, NANOG, SOX2 (FAM-labeled TaqMan probes, Life Technologies), and by flow cytometry for SSEA-3-PE, SSEA-4-PE, TRA-1-60-PE (eBioscience), respectively. Total RNA was extracted from iPSC using Nucleospin® RNA plus kit from Macherey-Nagel according to the manufacturer's protocol. Flow cytometry data were analyzed using FACSDiva software.

RRAD locus genotyping. Genomic DNA was extracted from iPSC lines using the Nucleospin® tissue kit (Macherey-Nagel). Briefly, the *RRAD* locus was amplified using forward primer (GTGTGGCCAGAACAGGAAAC) and reverse primer (GGACTCAAGCTGAGCCAAGA) under standard PCR conditions. The 560-bp PCR product was next visualized following agarose gel electrophoresis. *RRAD* locus was verified by classic sequencing with 3730 DNA Analyser (Applied Biosystems).

Cardiac differentiation of iPSCs and dissociation in single cells

Differentiation into cardiomyocytes. All iPSC lines were differentiated according to the matrix sandwich method (13). Before starting differentiation, iPSC colonies were transferred on stem cell-qualified Matrigel-coated plates (0.05 mg/mL; BD Biosciences) and cultured in StemMACS (iPS-Brew XF) medium (Miltenyi Biotec) with Y-27632 Rho kinase (ROCK) inhibitor (Stemcell Technologies) in a normal oxygen atmosphere. When the cells reached monolayer confluence, a second layer of the sandwich was added using cold IPS Brew with

Growth Factor Reduced Matrigel (0.066 mg/mL). The differentiation process was then initiated at day 0 following a protocol previously described (14).

iPSC-CMs dissociation. Twenty days after starting the differentiation, the iPSC-CMs were dissociated into single cells according to an established protocol (15). Briefly, the cells were enzymatically dissociated using Collagenase type 2 (295 U/mg; Gibco) for 20 minutes at 37°C. Next, dissociated cells were maintained at room temperature for 30 minutes in Kraft-Bruhe solution containing (in mmol/L): KCl, 85; K_2HPO_4, 30; $MgSO_4$, 5; EGTA, 1; Na_2-ATP, 2; Na-pyruvate, 5; creatinine, 5; taurine, 20; glucose, 20; pH adjusted to 7.2 with KOH. Finally, they were plated on stem cell-qualified Matrigel-coated Petri dishes (35 mm, Nunc^{TM}) in RPMI plus B27 supplement and 1% NEAA. Patch-clamp experiments were performed from 11 to 15 days after cell dissociation.

Genome Editing. The cells were transfected with CRISPR/Cas9 and single-stranded oligodeoxynucleotides using the Lipofectamine 3000 Reagent (Thermo Fisher Scientific). For each well of a 6-well plate, 2 εg CRISPR/Cas9 vectors and 4 εg single-stranded oligodeoxynucleotide were used for transfection. After clone picking and PCR product sequencing, several mutant clones were generated, 3 of which were continuously propagated and used for cardiomyocytes differentiation and characterization.

Neonatal mouse cardiomyocytes

Neonatal mouse cardiomyocytes isolation and culture. Single cell suspensions from 1-2 day-old mouse hearts were prepared in a semi-automated procedure by using the Neonatal Heart Dissociation kit and the gentleMACS^{TM} Dissociator (Miltenyi Biotec). After excision of the hearts from the mice, the ventricles were separated from the atria. After the gentle MACS program running, the cell supernatant was removed by centrifugation and the pellet was suspended in culture medium containing Dulbeccoôs modified Eagleôs medium (DMEM) supplemented with 10% horse serum, 5% foetal bovine serum and penicillin (100 U/mL)/

streptomycin (100 μg/mL). Then the cells were plated on 65-mm diameter Petri dishes (Nunc™). After 2 h of initial plating, the myocytes were suspended in the same culture medium and plated on 35-mm diameter Petri dishes at a density of 6 x 10^4 cells per plate.

Adenoviral infection of neonatal mouse cardiomyocytes. Adenoviruses encoding human WT-RAD plus GFP, R211H-RAD plus GFP and GFP alone (ad-WT-RAD, ad_R211H-RAD and ad-GFP, respectively) have been generated by Vector Biolabs after full-length cDNA of human *RRAD* was subcloned into Dual-U6 shuttle vector and checked by DNA sequencing. Adenoviral infection efficiency was assessed by measuring GFP fluorescence (510 nm) using fluorescence microscopy (Zeiss). Human Rad expression was quantified by RT-qPCR (FAM-labeled TaqMan probes, Life technologies) and Western Blot (Anti-RRAD antibody, Aviva Systems Biology). The potential cytotoxicity of the infection was evaluated by using non-invasive electrical impedance monitoring with the xCELLigence® RTCA DP apparatus (ACEA Biosciences, Inc). Based on these experiments, multiplicity of infection (MOI) of 10 then 100 viral particles *per* cell have been chosen for the three viruses. The cardiomyocytes were infected 24 hours after isolation in infection medium containing DMEM supplemented with 2% foetal bovine serum and penicillin (100 U/mL)/ streptomycin (100 μg/mL) for 2 hours. Patch-clamp experiments were performed 48 and 72 hours after infection.

Patch-clamp experiments

Data acquisition and analysis. Electrophysiological recordings were obtained on single cardiomyocytes (CMs) using an Axopatch 200B amplifier (Molecular Devices). Data were collected from a minimum of 3 independent differentiations per iPSC line and from at least 3 independent preparations of neonatal mouse CMs. Signals from I_{CaL} recordings were low-pass-filtered with a cut-off of 3 kHz and signals from I_{Na} recordings with a cut-off of 10 kHz. All recordings were analysed using Clampfit 10.4 software. The composition of all patch-clamp solutions is provided in the online supplementary Table 3.

Action potential. Action potential (AP) recordings were performed at 37°C using amphotericin-B-perforated-patch configuration of the patch-clamp technique on single CMs differentiated from iPSCs (iPSC-CMs). Pipettes (borosilicate glass, Sutter instruments) were pulled to obtain tip resistances of 2-3 MΩ. APs were recorded first at spontaneous rates, then at various pacing cycle lengths using 1.3-1.5-ms pulses of 300-1500 pA. Only ventricular APs were selected for further analysis based on their duration, maximum upstroke velocity (dV/dt_{max}), spontaneous cycle length, amplitude and maximum diastolic potential, as previously defined (14).

Current recordings. Whole-cell recordings of I_{CaL}, I_{Na} and I_{NaP} were obtained using the ruptured-patch configuration at 37°C, except for I_{Na} recording in the genome-edited and corresponding control iPSC-CMs, which was performed at 25°C. Wax-coated pipettes (borosilicate glass, Sutter instruments) were used with tip resistances of 1.5 to 2.5 MΩ. Capacitance and series resistances were compensated (60-70% compensation) to obtain minimal contribution of capacitive transients. Current densities were calculated by dividing current amplitude by membrane capacitance. The peak current-voltage (I/V) relationship and steady-state activation properties were evaluated using conventional voltage-clamp protocols which are shown as insets in figure 3. For determining steady-state inactivation properties of I_{Na}, cells were depolarized at -20 mV after 500-ms polarization to various potentials from -130 to -20 mV (holding potential: -100 mV; 10-mV increment; frequency 0.33 Hz). I_{Na} recovery from inactivation was investigated using a double 50-ms pulse to -20 mV (holding potential: -120 mV) protocol with an inter-pulse duration increasing from 1 to 1000 ms. Steady-state activation and inactivation curves were fitted using a Bolzmann equation. Time constants of inactivation of I_{Na} were determined by fitting a double exponential curve through the decay phase of the current.

Calcium imaging.

IPSC-CMs were dissociated and seeded in Matrigel-coated (BD bioscience) coverslips at a density of 20,000 cells per well. After recovery, cells were loaded with 5µM Fluo-4 AM in Tyrodeĝs solution (140 mM NaCl, 5.4 mM KCl, 1 mM MgCl2, 10 mM glucose, 1.8 mM CaCl2, and 10 mM HEPES pH = 7.4 with NaOH) for 10 min in incubator. Cells were then washed with pre-warmed Tyrodeĝs solution 3 times. Calcium signals were sampled by confocal microscope (Carl Zeiss,LSM 510 Meta, Göttingen, Germany) with a 63X oil-immersed objective (Plan-Apochromat 63x/1.40 Oil DIC M27). Signals were taken with line-scanning mode (512 pixels X 1920 lines).

Immunofluorescence staining and laser confocal microscopy.

Cell dissociation. iPSC-CMs were dissociated 20 days after starting the differentiation with type 2 collagenase (295 U/mg; Gibco) in Hankĝs Balanced Salt Solution and plated in 8 well chambered coverslips (Ibidi) coated with stem cell-qualified Matrigel. Immunofluorescent labelling was performed 12 days after dissociation.

Experiments on the family cell lines. iPSC-CMs maintained on Matrigel-coated glass coverslips were fixed with 4% paraformaldehyde (Thermo Fisher Scientific) for 15 min, permeabilized with 0.1% Triton X-100 (Sigma-Aldrich) for 15 min, and blocked with 1% BSA for 1 hr. After fixation, the cells were stained in PBS buffer containing 0.1% Triton X100 and 1% BSA In order to target only cardiomyocytes, we labelled Troponin I (Santa Cruz biotechnology) as a cardiac differentiation flag jointly with actin using Phalloidin Alexa Fluor 488 (Life technology). To study focal adhesion complexes we labelled Vinculin in iPSC-CM (Abcam). We used Alexa Fluor 488 and 560 corresponding species secondary antibodies purchased from Invitrogen and nuclei were highlighted by DAPI incubation. Photographs were obtained in collaboration with MicroPicell core facility (University of Nantes) using confocal microscopy (Nikon Eclipse A1), acquired with NIS element by Nikon and analysed with Fiji processor. For focal adhesion quantification the image was pre-analysed using Fiji than processed using the Focal Adhesion Analysis Server (16). For each experiment, 20 iPSC-CMs differentiated from 3 clones for the BrS1 patient, 2 clones for the Ctl1 individual and 1 clone for each additional family members (Ctl02 and BrS2) were used. For neonatal mouse cardiomyocytes, 8-10 cells per culture have been studied and 3 cultures have been performed.

Experiments on isogenic lines. iPSC-CMs maintained on Matrigel-coated glass coverslips were fixed with 4% paraformaldehyde (Thermo Fisher Scientific) for 15 min, permeabilized with 0.1% Triton X-100 (Sigma-Aldrich) for 15 min, and blocked with 1% BSA for 1 hr. After fixation, the cells were stained in PBS buffer containing 0.1% Triton X100 and 1% BSA with primary antibody dilutions for rabbit anti-cardiac troponin T (Abcam, ab45932) and mouse anti-Ŭ-actinin (Abcam, ab18061). Goat anti-rabbit Alexa 647 and goat anti-mouse Alexa 488 (Thermo Fisher Scientific) were used as secondary antibodies. After mounting with ProLong Gold Antifade mountant with DAPI (Thermo Fisher Scientific), imaging was performed using a Zeiss LSM 880 inverted confocal microscope using Zen imaging software. Cells with disorganized sarcomere were defined as having punctate Ŭ-actinin distribution without striations over 25% of cell area.

Rho kinase activity assay.

Rho kinase activity was measured on neonatal mouse cardiomyocytes overexpressing GFP (control), ad_WT-RAD or ad_R211H-RAD using the ROCK Activity Assay Kit from Cell Biolabs, Inc. The cells were dissociated at day 0, infected at day 1 and used at day 4. The cell lysate was first treated to extract total cytosolic protein fraction, which was used at a concentration of 50 µg per well for the assay.

Expression analysis

The expression at the transcriptional level of *RRAD* (Hs00188163_m1) and *SCN5A* (Hs00165693_m1) in the generated iPS-CMs was verified by RT-PCR using FAM-labeled TaqMan probes (Life Technologies).

The expression at the protein level of RAD was investigated in mouse and human ventricular myocardium. For mice, after euthanasia by cervical dislocation, the hearts were quickly excised and the right ventricle outflow track, the remaining right ventricle free wall and the left ventricle free wall were carefully dissected. Tissues were snap-frozen in liquid nitrogen, homogenized in ice-cold lysis buffer containing (in mmol/L): NaCl, 100; Tris-HCl, 50; EGTA, 1; 1% TritonX-100, Na3VO4, 1; NaF, 50; phenylmethylsulfonyl fluoride, 1 (Roche Applied Science); and protease inhibitor mixture (1:100 dilution; Sigma P8640) (pH 7.4). Extracted samples were sonicated and centrifuged at 15,000 × g for 15 min at 4°C. Total homogenate protein was quantified using the PierceÊ BCA Protein Assay Kit. Forty µg of total protein was used plus 2 µl of NuPAGE Sample Reducing Agent (Invitrogen) and 5 µl of NuPAGE LDS Sample Buffer (Invitrogen). The running was performed on 10% or 4-15% Mini-PROTEAN® TGX Stain-FreeTM Precast Gels (Bio-rad) and transferred on Trans-Blot® TurboÊ Nitrocellulose Transfer Packs (Bio-rad). Membranes were blocked (using 5% non-fat milk) and incubated using primary antibody (supplementary table 6). The secondary antibodies used were purchased from Santa Cruz and western blot revelation was performed using chemiluminescence camera (Biorad). Protein levels were quantified using image Lab software and normalized on stain free acquisition of the corresponding gels.

Nucleotide exchange assays

Full-length human WT-RAD and R211H-RAD were cloned in pET-28a(+) vector, expressed in *E. coli* and purified on Protino® Ni-NTA agarose beads (Macherey-Nagel).

Nucleotide exchange assay were performed as previously described (17). Briefly, all kinetics assays were carried out in a buffer containing 50 mM Tris at pH 8, 300 mM NaCl, 2 mM MgCl2, 1 mM DTT in the presence of 2 εM GTPases. GDP/GTP exchange reactions were started by addition of 40 εM *N*-methylanthraniloy-GTP (mant-GTP, JenaBiosciences, Jena Germany). Nucleotide exchange kinetics were performed either without EDTA for spontaneous GDP/GTP exchange or with 0,5 εM EDTA for single k_{obs} (s^{-1}) determination. Nucleotide exchange kinetics were monitored by GDP/mant-GTP exchange using the fluorescence of the mant fluorophore (∂exc=360 nm, ∂em=440 nm) with a Victor multilabel plate reader (Perkin Elmer) at RT. The k_{obs} was determined from single-exponential fit of the fluorescence change.

Statistics

Data are expressed as mean ± SD in the text of the manuscript and in tables. In figures, data are presented as box plots, except in current density/voltage curves where they are presented as mean ± SEM. Statistical analysis was performed with Prism5 (GraphPad Software, Inc.) or SigmaPlot 12.5 (Systat Software, Inc.). Statistically significant differences were determined with Mann-Whitney rank sum test for comparison of two groups. For more than two groups, Kruskal-Wallis rank sum test or two-way analysis of variance were performed with Bonferroni post-hoc test for multiple comparisons when appropriate. Fisher exact test or Khi2 test were used for proportions comparisons. The tests used are mentioned in the figure legends. A p value of 0.05 or less indicated significance.

Online supplementary results

iPSC reprogramming and differentiation

PBMCs isolated from blood samples from the proband (BrS1) and from his unaffected brother (Ctl1) were reprogrammed into iPSCs upon infection with Sendai virus. Two Ctl1 iPSC clones (Ctl103 and Ctl104) and three BrS1 clones (BrS101, BrS102 and BrS103) were characterized (Online supplementary figure 2). Integrity and transmission of the *RRAD* gene during reprogramming process was assessed. The sequencing results confirmed that iPSC reprogrammed from the proband carried the *RRAD* p.R211H variant while control iPSC carried the WT sequence of *RRAD* gene (Online supplementary figure 2B). qRT-PCR analysis confirmed that both iPSC types were free from Sendai virus carrying the reprogramming factors sequences (Online supplementary Figure 2D). Endogenous expression of the pluripotent stem cells markers, OCT4, NANOG and SOX2 was detected by qRT-PCR at level comparable to H9 human embryonic stem cells (Online supplementary figure 2E). Endogenous expression of OCT3/4 and TRA-1-60 proteins was also visualized by immunofluorescence staining (Online supplementary Figure 2A) and flow cytometry analysis showed that more than 80% of Ctl and BrS iPSC were positive for the expression of pluripotency markers SSEA3, SSEA4 and TRA-1-60 (Online supplementary figure 2C). Single-nucleotide polymorphism (SNP) analysis (molecular karyotypes) revealed that Ctl and BrS iPSC clones did not present genomic duplication or deletion as compared to parental PBMCs (data not shown). Finally, the ability of both iPSC types to differentiate into cardiomyocytes was verified, with comparable Troponin I expression and organization in striations (Online supplementary figure 2F).

An additional affected family member carrying the *RRAD* variant recapitulates the BrS phenotype observed in the probandôs iPSC-CMs.

In order to confirm the involvement of the mutation in the phenotype observed in the iPSC-

CMs derived from the proband, we derived iPSC-CMs from the proband's daughter (individual IV:2) carrying the variant and positive for BrS after flecainide test. The results obtained were compared with the corresponding control cell line (Ctl2) which was derived from her unaffected sister (individual IV:1) who does not carry the mutation. As shown in online supplementary figure 4A-D both I_{Na} and I_{caL} densities were significantly lower (by 43% and 20% at -25 mV and 0 mV respectively) in BrS2 iPSC-CMs than in Ctl2 iPSC-CMs. Steady-state activation and inactivation, as well as recovery from inactivation properties of the sodium current did not differ between BrS2 and Ctl2 iPSC-CMs (Online supplementary table 4).

Human RAD GTPase overexpression in neonatal mouse cardiomyocytes recapitulates BrS iPSC-CMs phenotype

In order to check whether the *RRAD* p.R211H variant was indeed responsible for both electrical and cytoskeletal anomalies, we investigated the effects of an adenoviral expression of either GFP alone (ad_GFP), wildtype human RAD plus GFP (ad_WT-RAD), or p.R211H-RAD plus GFP (ad_R211H-RAD), in neonatal mouse cardiomyocytes in primary culture. At MOI 10, ad_WT-RAD and ad_GFP cells exhibited comparable I_{Na} density whereas ad_R211H-RAD showed a 30% reduction of I_{Na} density (Online supplementary figure 10) without disturbance of biophysical properties (Online supplementary Table 5). Interestingly, when the adenovector MOI was increased by 10-fold, ad_WT-RAD cells also displayed a severe reduction of I_{Na} density while I_{Na} density in ad_R211H-RAD cells was further decreased. These results suggest that the variant induces a gain of function of RAD (Online supplementary figure 10C). Furthermore, ad_R211H-RAD cells exhibited similar alterations in F-actin organization and cell shape abnormalities as observed in BrS iPSC-CMs (Online supplementary figure 11). These results could be linked to the reduction of Rho kinase activity in ad_R211H-RAD cardiomyocytes compared to ad_WT-RAD and ad_GFP cells, while its expression was not altered (Online supplementary figure 12).

Online supplementary figures

Supplementary figure 1. ECG recordings of the patient III:8. A. DII peripheral lead and V1-V6 precordial leads ECG recordings under baseline condition. V1 and V2 were recorded in the 4th intercostal space **B.** V1-V3 leads ECG recordings under flecainide challenge.

Supplementary figure 2. Pluripotency validation and cardiac differentiation of the reprogrammed induced pluripotent stem cell (iPSC) lines. A. Representative Immunostaining of membrane pluripotency markers TRA-1-60 (FITC), nuclear pluripotency marker OCT4 (Rhodamine), DAPI and merged image for iPSC colonies obtained from the proband (BrS1) and his unaffected brother (Ctl1). **B.** Sequencing of p.R211H-*RRAD* locus in both Ctl and BrS iPSC lines. **C.** FACS quantification of pluripotency markers SSEA3, SSEA4 and TRA-1-60 in both Ctl (white) and BrS (black) iPS cell lines. **D.** Expression of SEV transcript expressed by Sendai virus. Passage 2 reprogramming intermediates were used as positive control (iPSC P2 in white); human embryonic stem cells (hESC; in black) and passage 13 iPSCs (iPSC P13; in white) were used as negative controls. **E**. mRNA expression of pluripotency markers OCT4, NANOG and SOX2 in the same cell groups. **F.** Troponin I labelling (Rhodamine) in cardiomyocytes derived from Ctl and BrS iPSCs as a marker for cardiac differentiation. Scale bar, 10 µm.

Supplementary figure 3. Nav1.5 protein levels in iPSC-CMs obtained from the proband (BrS1) and his unaffected brother (Ctl1). A. Representative Western blot of Nav1.5 in Ctl1 and BrS1 iPSC-CMs. **B.** Corresponding box plot of Nav1.5 expressions normalized to stain free. Statistical test: Mann-Whitney rank sum test.

Supplementary figure 4. An additional member of the family carrying the RRAD variant with Brugada syndrome recapitulates the electrophysiological phenotype. A. Superimposed representative I_{Na} (A) traces recorded in Ctl2 and BrS2 iPSC-CMs. **B.** Mean

(±SEM) current density-voltage relationship in Ctl2 and BrS2 iPSC-CMs (*p<0.05, **p<0.01; Two Way ANOVA with Bonferroni post-hoc test for multiple comparisons). **C.** Superimposed representative $I_{Ca,L}$ (C) traces recorded in Ctl2 and BrS2 iPSC-CMs. **D.** Mean (±SEM) current density-voltage relationship in Ctl2 and BrS2 iPSC-CMs (*p<0.05, **p<0.01, ***p<0.001; two-way analysis of variance with Bonferonni post-hoc test for multiple comparisons). **E.** Representative action potential recording of spontaneously beating BrS2 iPSC-CMs.

Supplementary figure 5. Sodium and calcium currents in cardiomyocytes differentiated from the different clones of induced pluripotent stem cells (iPSCs) obtained from the proband (BrS1) and his unaffected brother (Ctl1). A-B. I_{Na} (A) and I_{CaL} (B) current density-voltage relationships for the cardiomyocytes differentiated from 2 Ctl1 iPSC clones (Ctl103 and Ctl104) and from 3 BrS1 iPSC clones (BrS101, BrS102 and BrS103). See Figure 3 for voltage-clamp protocols.

Supplementary figure 6. Action potentials in cardiomyocytes differentiated from the different clones of induced pluripotent stem cells (iPSCs) obtained from the proband (BrS1) and his unaffected brother (Ctl1). A. Representative action potential recordings of spontaneously beating cardiomyocytes differentiated from Ctl1 iPSC clones 1 and 2 (Ctl103 and Ctl104) and from BrS1 iPSC clones 1, 2 and 3 (BrS101, BrS102 and BrS103). **B-C**. Box plots of maximum upstroke velocity (B; dV/dT_{max}) and peak to peak duration (C) of spontaneous action potentials. Statistical test: Kruskal-Wallis rank sum test (*versus* Ctl104). **D**. Representative action potentials recorded at a pacing cycle length of 700 ms in Ctl and BrS01-03 iPSC-CM lines. **E.** Box plot of action potential duration at 30% (APD30), 50% (APD50) and 90% (APD90) of full repolarization. Two-way analysis of variance with Bonferonni post-hoc test for multiple comparisons (*versus* Ctl104).

Supplementary figure 7. Focal adhesions in cardiomyocytes differentiated from induced pluripotent stem cells obtained from the proband (BrS1) and his unaffected brother

(Ctl1). Top. Representative images of immunostaining of vinculin (FITC), troponin I (rhodamine) and merged acquisitions with DAPI. **Bottom.** Box plot of the number of focal adhesion per cell. Statistical test: Mann Whitney rank sum test.

Supplementary figure 8. An additional member of the family carrying the RRAD variant with Brugada syndrome recapitulates the structural phenotype. Top. Representative 3D acquisition of immunostainings of filamentous actin (F-actin; stained with phalloidin, FITC) and troponin I (rhodamine) and merged acquisitions with nucleus staining with DAPI in Ctl2 and BrS2 iPSC-CMs (Width: 107.12 µm; height: 12 µm; Depth: 107.12 µm)**. Bottom.** Representative images of immunostaining of vinculin (FITC), troponin I (rhodamine) and merged acquisitions with DAPI. Scale bars: 25 µm.

Supplementary figure 9. A. Genome edited cell line inserted with RRAD R211H variant. **A.** Insertion of *RRAD* mutation using CRISPR/Cas9 genome-editing tool**. (a)** Sequencing chromatogram shows a wildtype *RRAD* (C/C) and CRISPR edited mutant *RRAD* (T/T) at nucleotide position chr16:66957436 in a human iPSC line. The wildtype allele *C* is substituted by *T* after genome-editing as shown in the lower panel. **(b)** Schematic of the strategy for precise genome modification using CRISPR/Cas9 and the homologous repair oligo to generate isogenic *RRAD T/T* mutant iPSC lines. CRISPR/Cas9 specifically cleaves near the nucleotide position Chr16 66957436 at exon 3 at the *RRAD* locus. The sequence of guide RNA for Cas9 is shown in blue and the Cas9 cutting site is pointed by the thinner arrow. The nucleotide sequence in yellow indicates the PAM motif required for Cas9 cleavage. The *RRAD* mutation position is shown in bold red. HR: homologous repair. **B.** Mean (±SEM) current-voltage relationship for calcium current recorded on both Rad WT and Rad R211Hins. **C.** Representative examples of Troponin T (red) and Actinin (green) immunostaining performed on Rad WT and Rad R211H ins cardiomyocytes acquired using confocal microscopy. Scale bar = 20 µM.

Supplementary figure 10. I_{Na} in neonatal mouse cardiomyocytes transduced with

adenoviruses encoding green fluorescence protein alone (ad_GFP), wildtype human RAD plus GFP (ad_WT-RAD), or human RAD carrying the variant p.R211H (ad_R211H-RAD). A. Superimposed representative I_{Na} (A) traces from ad_GFP, ad_WT-RAD and ad_R211H-RAD cardiomyocytes. Voltage-clamp protocols are shown in insets. **B.** Current density-membrane voltage relationship of I_{Na} recorded in ad_GFP, ad_WT-RAD and ad_R211H-RAD cardiomyocytes. *p<0.05, **p<0.01 (two-way analysis of variance with Bonferroni post-hoc test for multiple comparisons). **C.** Maximum current density of I_{Na} recorded in ad_GFP, ad_WT-RAD and ad_R211H-RAD cardiomyocytes infected with an MOI of 10 (unfilled bars), and ad_WT-RAD and ad_R211H-RAD cardiomyocytes infected with an MOI of 100 (filled bars). Statistical test: Kruskal-Wallis rank sum test (*versus* ad_WT-RAD).

Supplementary figure 11. Cytoskeleton in neonatal mouse cardiomyocytes transduced with adenoviruses encoding Green Fluorescence Protein alone (ad_GFP), GFP and wildtype *RRAD* (ad_WT-RAD) or GFP and *RRAD* R211H variant (ad_R211H-RAD). A. Representative images of GFP fluorescence (indicating the transduced cardiomyocytes), F-actin cytoskeleton staining with phalloidin and merged acquisitions with DAPI for each condition. Scale bars: 50 µm. Right panels are zoomed views of the merged images. **B.** Corresponding F-actin fluorescence distribution measured at the level of the yellow dotted lines. **C.** Cell size quantification and comparison for each group (GFP n=32, WT-Rad n=28, Rad R211H n=22). Statistical test: Mann Whitney rank sum test.

Supplementary figure 12. Rho kinase (ROCK) expression and function in neonatal mouse cardiomyocytes transduced with adenoviruses encoding green fluorescence protein alone (ad_GFP), GFP and wildtype *RRAD* (ad_WT-RAD) or GFP and *RRAD* R211H variant (ad_R211H-RAD). A. Representative western blots showing human RAD and mouse Rock expression in the three experimental conditions, with corresponding stain free membrane. The graphs show the mean ± SEM RAD and Rock expression (normalized to stain free). **B.** Western blot with corresponding stain free membrane showing mouse myosin phosphatase targeting protein (MYPT) and phospho-MYPT expression in the three experimental conditions. **C.** Rho kinase activity assay results for MYPT phosphorylation levels in each condition. For all panels, the number of cell isolations per experimental condition was 3. Statistical test: Mann Whitney rank sum test.

References

1. Priori SG, Wilde AA, Horie M, et al. HRS/EHRA/APHRS Expert Consensus Statement on the Diagnosis and Management of Patients with Inherited Primary Arrhythmia Syndromes: Document endorsed by HRS, EHRA, and APHRS in May 2013 and by ACCF, AHA, PACES, and AEPC in June 2013. *Heart Rhythm* 2013;10:1932-63.
2. Therasse D, Sacher F, Petit B, et al. Sodium-channel blocker challenge in the familial screening of Brugada syndrome: Safety and predictors of positivity. *Heart Rhythm* 2017;(July). doi:10.1016/j.hrthm.2017.06.031.
3. Coffey AJ, Kokocinski F, Calafato MS, et al. The GENCODE exome: sequencing the complete human exome. *Eur J Hum Genet* 2011;19:827-31.
4. Portero V, Le Scouarnec S, Es-Salah-Lamoureux Z, et al. Dysfunction of the voltage-gated K^+ channel β2 subunit in a familial case of Brugada syndrome. *J Am Heart Assoc* 2016;5:e003122.
5. McLaren W, Gil L, Hunt SE, et al. The Ensembl Variant Effect Predictor. *Genome Biol* 2016;17:122.
6. Lek M, Karczewski KJ, Minikel E V, et al. Analysis of protein-coding genetic variation in 60,706 humans. *Nature* 2016;536:285-91.
7. Kumar P, Henikoff S, Ng PC. Predicting the effects of coding non-synonymous variants on protein function using the SIFT algorithm. *Nat Protoc* 2009;4:1073-1081.
8. Adzhubei IA, Schmidt S, Peshkin L, et al. A method and server for predicting damaging missense mutations. *Nat Methods* 2010;7:248-9.
9. Kircher M, Witten DM, Jain P, et al. A general framework for estimating the relative pathogenicity of human genetic variants. *Nat Genet* 2014;46:310-5.
10. Lindenbaum P, Le scouarnec S, Portero V, Redon R. Knime4Bio: A set of custom nodes for the interpretation of next-generation sequencing data with KNIME. *Bioinformatics*

2011;27:3200-1.

11. Han L, Abney M. Identity by descent estimation with dense genome-wide genotype data. *Genet Epidemiol*. 2011;35:557-67.
12. Morgenthaler S, Thilly WG. A strategy to discover genes that carry multi-allelic or mono-allelic risk for common diseases: a cohort allelic sums test (CAST). *Mutat Res*. 20073;615:28-56.
13. Zhang J, Klos M, Wilson GF, et al. Extracellular matrix promotes highly efficient cardiac differentiation of human pluripotent stem cells: The matrix sandwich method. *Circ Res* 2012;111:1125-36.
14. Jouni M, Si-Tayeb K, Es-Salah-Lamoureux Z, et al. Toward personalized medicine: Using cardiomyocytes differentiated from urine-derived pluripotent stem cells to recapitulate electrophysiological characteristics of type 2 long QT syndrome. *J Am Heart Assoc* 2015;4:1-13.
15. Terrenoire C, Wang K, Chan Tung KW, et al. Induced pluripotent stem cells used to reveal drug actions in a long QT syndrome family with complex genetics. *J Gen Physiol* 2013;141:61-72.
16. Berginski ME, Gomez SM. The Focal Adhesion Analysis Server: a web tool for analyzing focal adhesion dynamics. *F1000Research* 2013;2:68.
17. Ferrandez Y, Zhang W, Peurois F, Akendengué L, Blangy A, Zeghouf M & Cherfils J. Allosteric inhibition of the guanine nucleotide exchange factor DOCK5 by a small molecule. *Scientific Report.* 2017; 7-1440.

Online supplementary table 1. Rare variants shared by the 5 affected family members

Gene variant	***RRAD***	***FHOD1***	***SPTBN5***	***SPTBN5***	***SNAP23***	***H6PD***
Variant position, allele frequency and predicted pathogenicity						
Genomic position (hg19)	chr16:66957436 C>T	chr16:67268268 C>T	chr15:42159782 C>T	chr15:42168786 T>C	chr15:42823617 A>G	chr1:9324684 A>G
HGVSp	NP_004156.1: p.Arg211His	NP_037373.2: p.Gly476Glu	NP_057726.4: p.Arg2089His	NP_057726.4: p.Glu1304Gly	NP_570710.1: p.Thr140Ala	NP_004276.2: p.Asp711Gly
ExAC AF (v0.3.1)	8.274e-6 (1/120860)	1.313e-4 (14/106658)	8.282e-6 (1/120746)	Absent	8.291e-6 (1/120614)	3.028e-4 (36/118900)
gnomAD AF (v2.0)	4.125e-6 (1/242446)	1.077e-4 (29/269262)	2.526e-5 (7/277126)	1.12e-5 (3/267860)	8.913e-6 (2/224396)	3.484e-4 (96/275570)
GERP score	4.81	4.22	-1.33	0.1	3.31	5.62
CADD PHRED score	33	11.84	9.98	15.05	19.65	22.3
PolyPhen-2/ SIFT	probably damaging/ deleterious	benign/ tolerated	benign/ -	benign/ -	benign/ tolerated	benign/ tolerated
Familial segregation						
II:2 (U)	+/-	+/-	+/-	+/-	+/-	+/-
II:5 (U)	-/-	-/-	+/-	+/-	+/-	-/-
III:1 (U)	-/-	-/-	+/-	+/-	+/-	+/-
III:2 (A)	+/-	+/-	+/-	+/-	+/-	+/-
III:4 (U)	+/-	+/-	-/-	-/-	-/-	+/-
III:5 (A)	+/-	+/-	+/-	+/-	+/-	+/-
III:6 (A)	+/-	+/-	+/-	+/-	+/-	+/-
III:7 (A)	+/-	+/-	+/-	+/-	+/-	+/-
III:8 (U)	+/-	+/-	-/-	-/-	-/-	-/-
III:9 (U)	-/-	-/-	-/-	-/-	-/-	-/-
III:10 (U)	-/-	-/-	+/-	+/-	+/-	-/-
III:11 (U)	-/-	-/-	+/-	+/-	+/-	-/-
IV:1 (U)	-/-	-/-	+/-	+/-	+/-	+/-
IV:2 (A)	+/-	+/-	+/-	+/-	+/-	+/-

AF: allele frequency. A: affected, U: unaffected (see Figure 1B and Table 1). CADD scores were obtained from http://cadd.gs.washington.edu/download. Mutational status could not be determined for individuals I:1, I:2, II:1, II:3, II:4, II:6 and III:3 (no DNA available).

Online supplementary table 2. *RRAD* rare variants in 186 Brugada index cases and 856 control individuals

	***RRAD* variants in BrS cases**			***RRAD* variants in controls**		
Carriers	1st case (isolated case)	2nd case (isolated case)	3rd case (isolated case)	1st control		2nd control
Age at diagnosis	46 yo	35 yo	37 yo	N/A		N/A
Genomic position (hg19)	chr16:66958947 C>A	chr16:66957511 T>C	chr16:66957425 C>T	chr16:66956194 G>C	chr16:66956195 G>T	chr16:66956161 G>A
HGVSp (NP_004156.1)	p.Asp46Tyr	p.Gln186Arg	p.Val215Met	p.His237Gln	p.His238Asp	p.Arg249Cys
ExAC AF (v0.3.1)	-	4.944e-5 6/121358	1.669e-5 2/119846	-	-	-
gnomAD AF (v2.0)	-	4.468e-5 11/246168	2.077e-5 5/240752	-	-	-
GERP score	4.38	4.81	3.83	5.8	2.42	5.93
CADD PHRED score	32	24.6	22.7	25.8	15.74	34
PolyPhen-2/ SIFT	possibly damaging/ deleterious	probably damaging/ tolerated	benign/ tolerated	benign/ tolerated	probably damaging/ deleterious	probably damaging/ deleterious

AF: allele frequency. Screening for rare variants was performed by Sanger sequencing in cases and whole-genome sequencing in controls (mean depth 37x for the 927 coding bases of *RRAD*). CADD scores were obtained from https://cadd.gs.washington.edu/snv (GRCh37-v1.4).

RRAD variants were identified in 3/186 BrS cases and 2/856 controls.

Online supplementary table 3. Composition of patch-clamp solutions (in mmol/L).

	Tyrode	**Action potential int.**	**I_{CaL} int.**	**I_{CaL} ext.**	**iPSC-CMs**			**NM-CMs**	
					I_{Na} int.	**I_{Na} ext.**	**I_{NaP} ext.**	**I_{Na} int.**	**I_{Na} ext.**
NaCl	140	5	5		3	20	130	5	25
KCl	4	20							
CsCl			145		133	110	10	105	94
TEA-Cl				160	2				25
$CaCl_2$	1		2	5				4	1
$MgCl_2$	1			1	2	1	1		2
$CoCl_2$						1.8	1.8		2.5
K-gluconate		125							
Na_2ATP					2				
MgATP			5					5	
EGTA			5		5			10	
HEPES	10	5	10	10	5	10	10	10	10
glucose	10			10		10	10	5	
mannitol				20		20	20		20
Tetrodotoxin				0.03					
Amphotericin B		0.85							
pH **(adjusted with)**	7.4 (NaOH)	7.2 (KOH)	7.2 (CsOH)	7.4 (CsOH)	7.2 (CsOH)	7.4 (CsOH)	7.4 (CsOH)	7.2 (CsOH)	7.4 (CsOH)

Abbreviations are: int., intrapipette solution; ext., extracellular medium; iPSC-CMs, induced pluripotent stem cell-derived cardiomyocytes; NM-CMs, neonatal mouse cardiomyocytes; TEA-Cl, tetraethylammonium chloride.

Online supplementary table 4. Biophysical properties of I_{Na} and $I_{Ca,L}$ recorded in cardiomyocytes derived from iPS cells from the family control (Ctl1, Ctl2) and diseased (BrS1, BrS2) members and from iPS isogenic control (Rad-WT) and knock-in (Rad R211H ins) cell lines.

	Group	Activation		Inactivation		Recovery from inactivation		
		$V_{1/2}$(mV)	K	$V_{1/2}$ (mV)	K	Űf (ms)	Af (%)	Űs(ms)
I_{Na}	**Ctl1**	-39.4±5.3 (n=17)	5.3±0.8	-83.4±5.3	5.3±0.4	9.7±2.1 (n=13)	67.7±5.05	109.1±24.5
	BrS1	-36.1±4.5 (n=42)	5.2±1.2	-82.9±5.1	4.5±3.8	6.7±2.3** (n=33)	68.4±7.47	93.6±18.9
	Ctl2	-35.2±2.6 (n=11)	5.4±0.6	-84.1±3.6	5.2±0.9	9.2±3.4 (n=7)	52.9±17.7	121.1±26.2
	BrS2	-35.9±3.1 (n=10)	6.2±1.6	-82.9±3.8	5.0±1.5	9.2±3.7 (n=7)	53.6±18.9	119.9±19.3
	# **Rad WT**	-35.1±4.8 (n=18)	6.3±1	-86.3±4.7	5.8±0.7	48.2±12.0 (n=14)	75.7±8.3	541.1±183.3
	# **Rad R211H ins**	-32.8±2.6 (n=14)	6.5±1.4	-86.4±5.4 (n=13)	5.8±0.5	32.5±9.7** (n=11)	71.2±10.3	367.4±134.2*

	Group	Activation	
		$V_{1/2}$ (mV)	K
I_{CaL}	**Ctl1**	-18.6±3.5 (n=34)	5.5±0.6
	BrS1	-18.6±2.9 (n=24)	5.8±0.5
	Ctl2	-19.1±3.2 (n=12)	5.4±0.7
	BrS2	-18.2±2.8 (n=15)	6.2±1.0
	Rad WT	-18.6±2.9 (n=16)	6.1±0.9
	Rad R211H ins	-16.2±3.3 (n=16)	6.3±0.6

Data are given as mean ± SD. Abbreviations: $V_{1/2}$, voltage for half-activation or half-inactivation; K, slope of steady-state activation or inactivation curves; Űf, Űs, time constants of the fast and slow components, respectively, of recovery from inactivation; Af, coefficient of the fast component of recovery from inactivation. $^{\#}$, I_{Na} recording in RAD WT and Rad R211H ins iPSC-CMs were performed at 25°C; $^{**}p<0.01$, $^{***}p<0.001$ *versus* corresponding control.

Online supplementary table 5. Biophysical properties of I_{Na} in neonatal mouse cardiomyocytes infected with an adenovirus coding for GFP (Ad_GFP) alone or GFP and wildtype human *RRAD* (Ad_WT-RAD) or GFP and p.R221H human *RRAD* (Ad_R211H-RAD).

Condition	Activation		Inactivation	
	$V_{1/2}$	K	$V_{1/2}$	K
Ad_GFP (MOI 10) **n=6**	-46.2±2.9	6.6±1.9	-94.9±2.6	5.4±2.4
Ad_WT-RAD (MOI 10) **n=7**	-46.2±2.9	5.0±1.0	-86.8±3.7	7.7±1.6
Ad_R211H-RAD (MOI 10) **n=6**	-41.6±1.9	5.0±2.2	-81.7±9.3	6.6±0.7

Data are given as mean±SD. Abbreviations: $V_{1/2}$, voltage for half-activation or half-inactivation; K, slope of steady-state activation and inactivation curves.

Online supplementary table 6. Primary antibodies used for protein quantification by western blot.

Protein	Host	Producer	Reference
RAD	Rabbit	Aviva System Biology	ARP-56566
$Na_V1.5$	Rabbit	Cell Signalling	D9J7S
ROCK 2	Rabbit	Abcam	ab71598
MYPT	Rabbit	Santa Cruz	sc25618
p-MYPT	Rabbit	Santa Cruz	sc17556R

Online supplementary figure 1

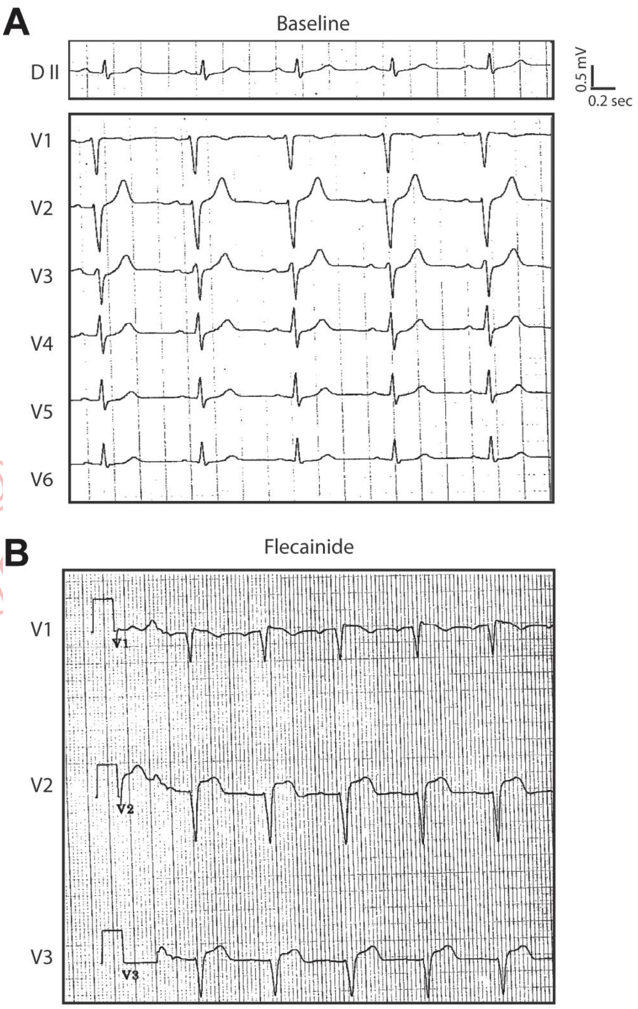

Online supplementary figure 2

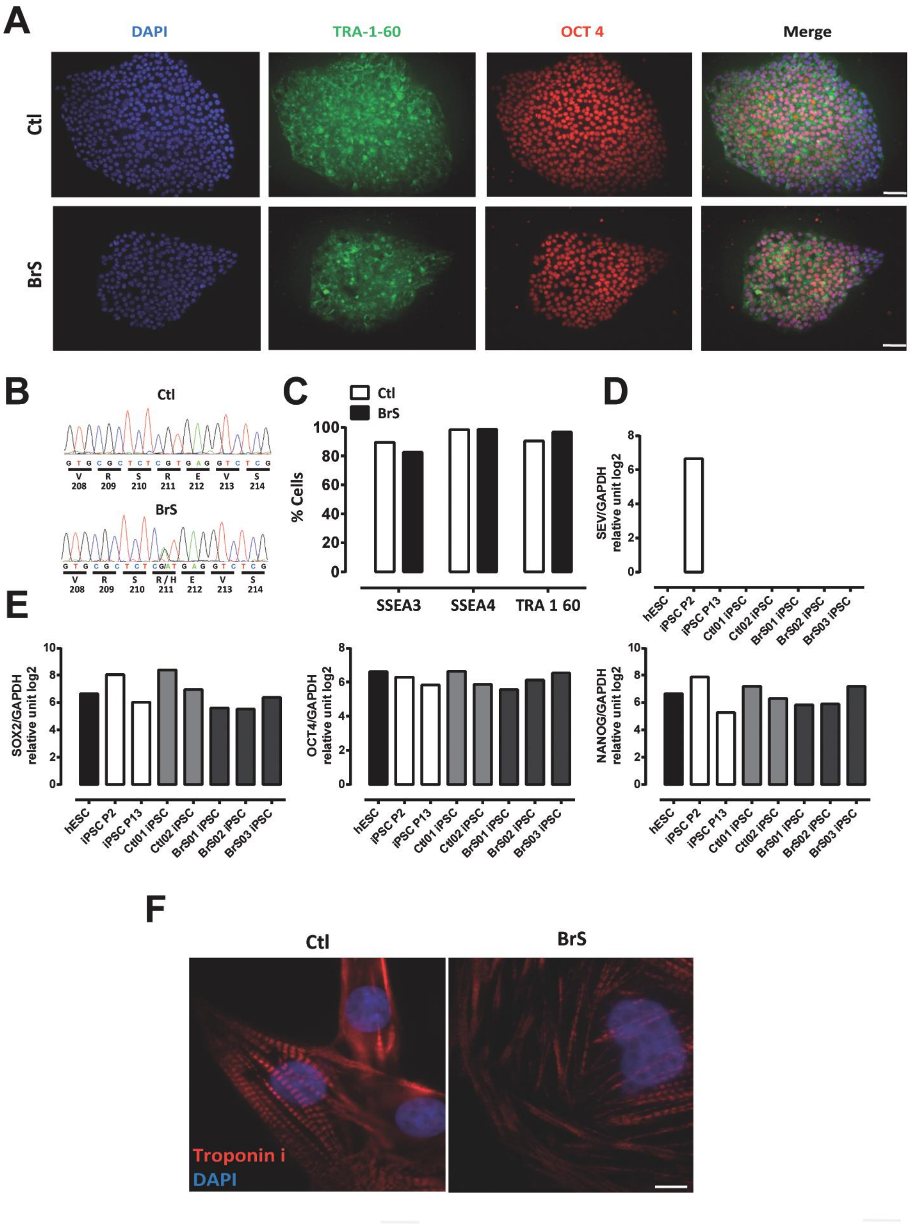

Online supplementary figure 3

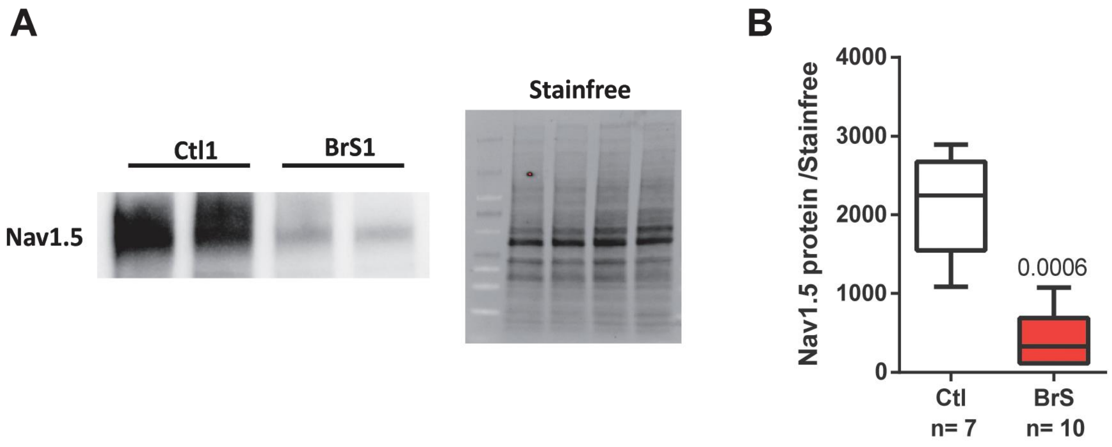

Online supplementary figure 4

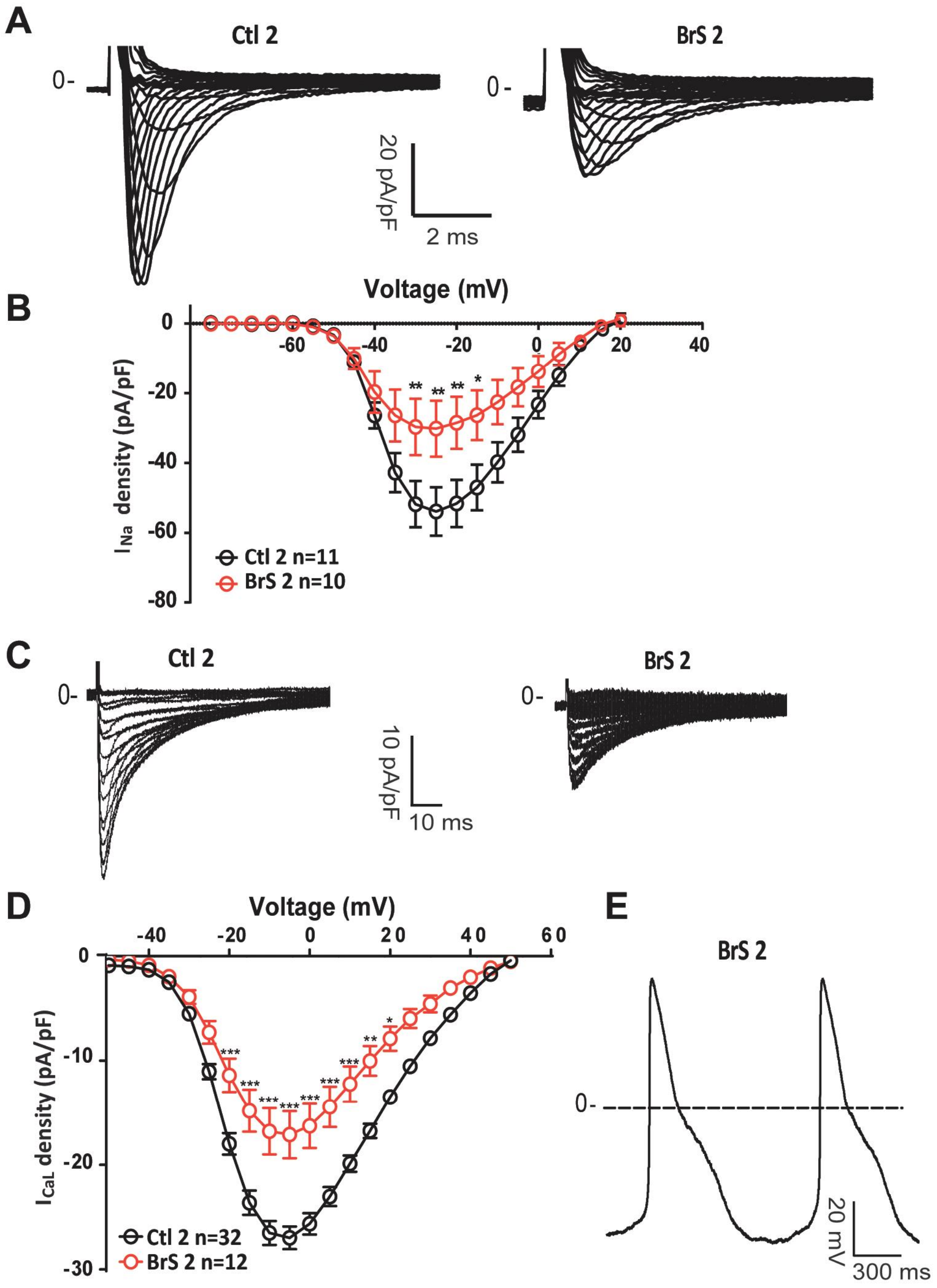

Online supplementary figure 5

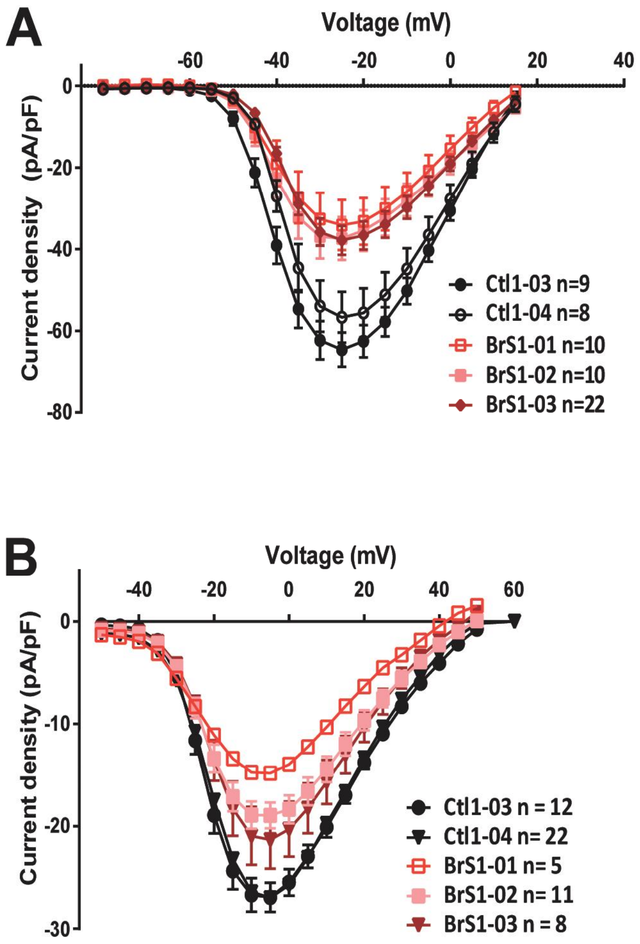

Online supplementary figure 6

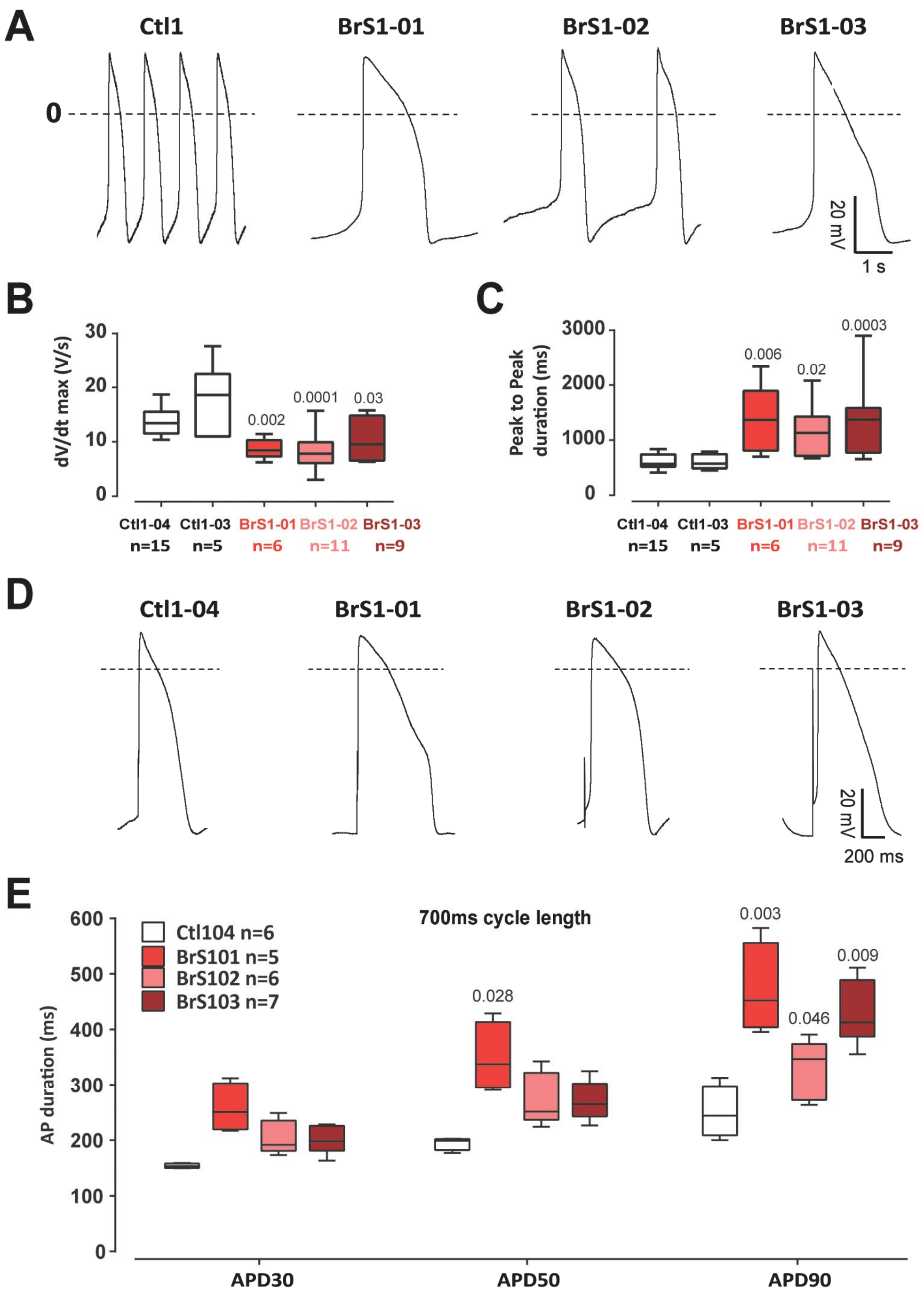

Online supplementary figure 7

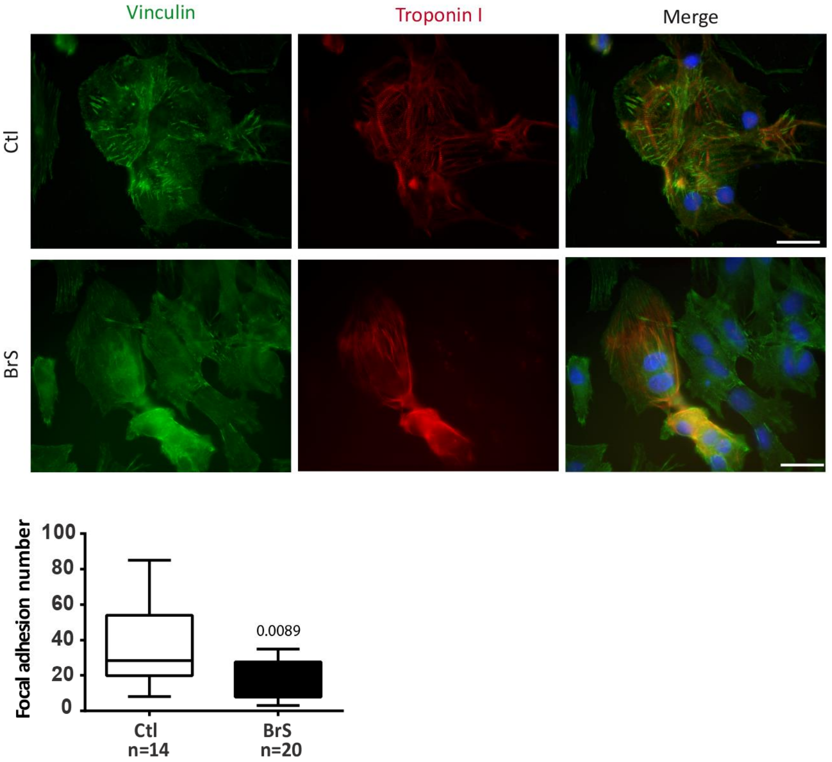

Online supplementary figure 8

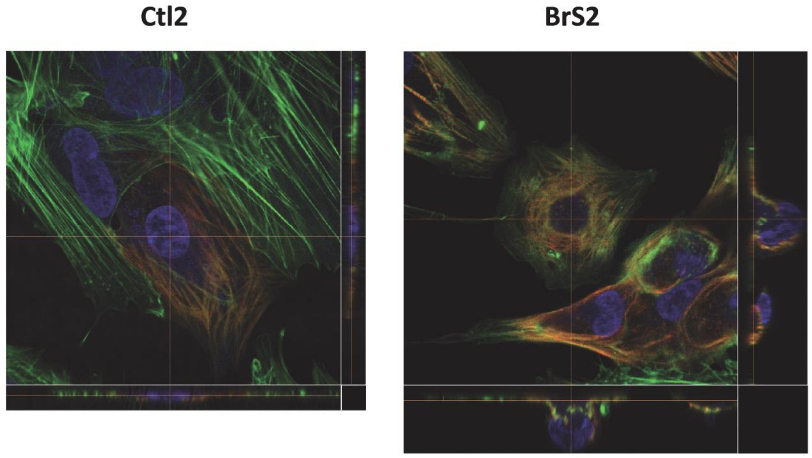

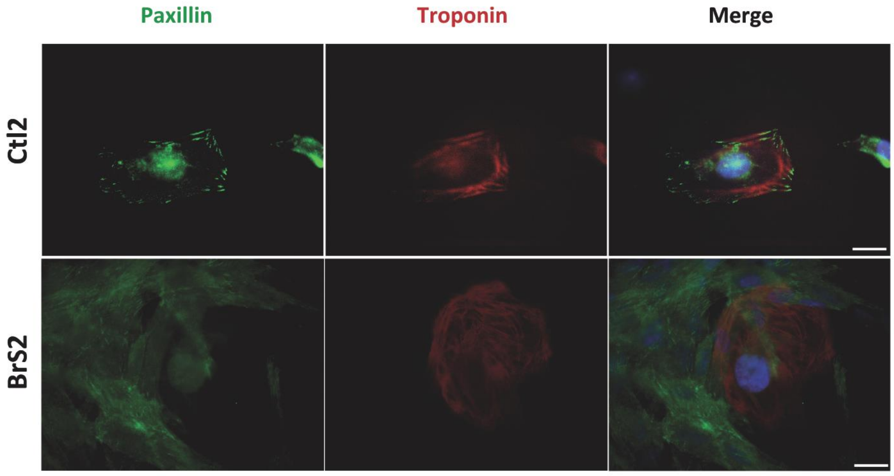

Online supplementary figure 9

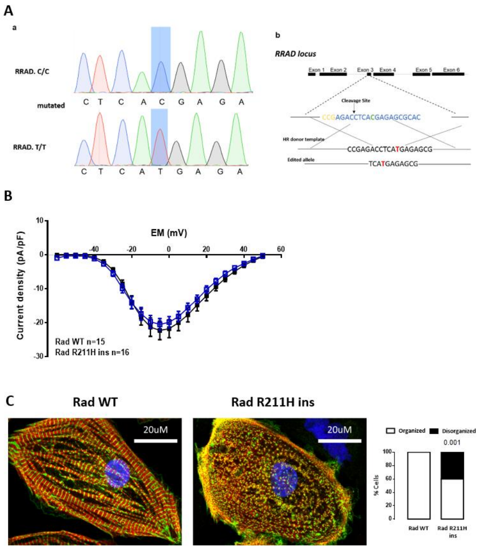

Online supplementary figure 10

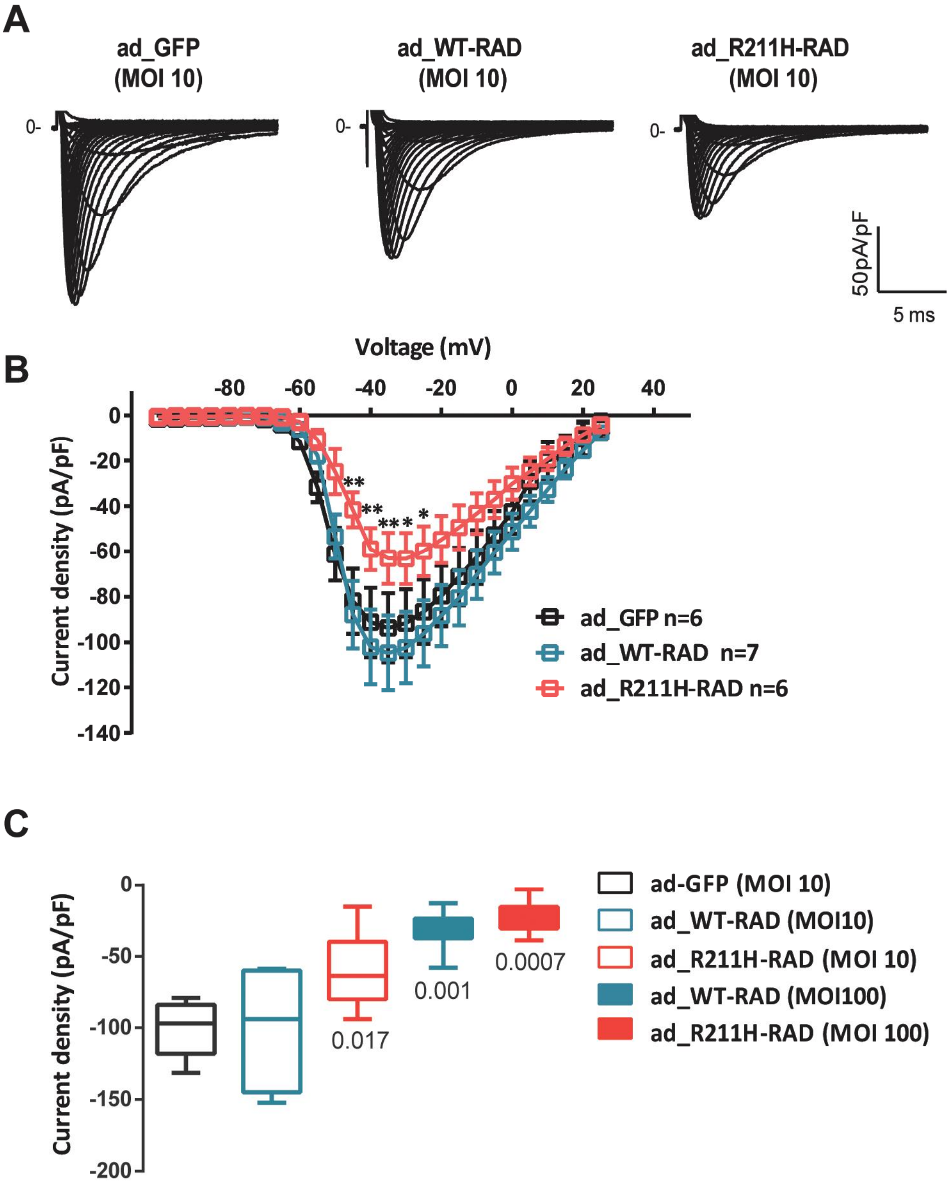

Online supplementary figure 11

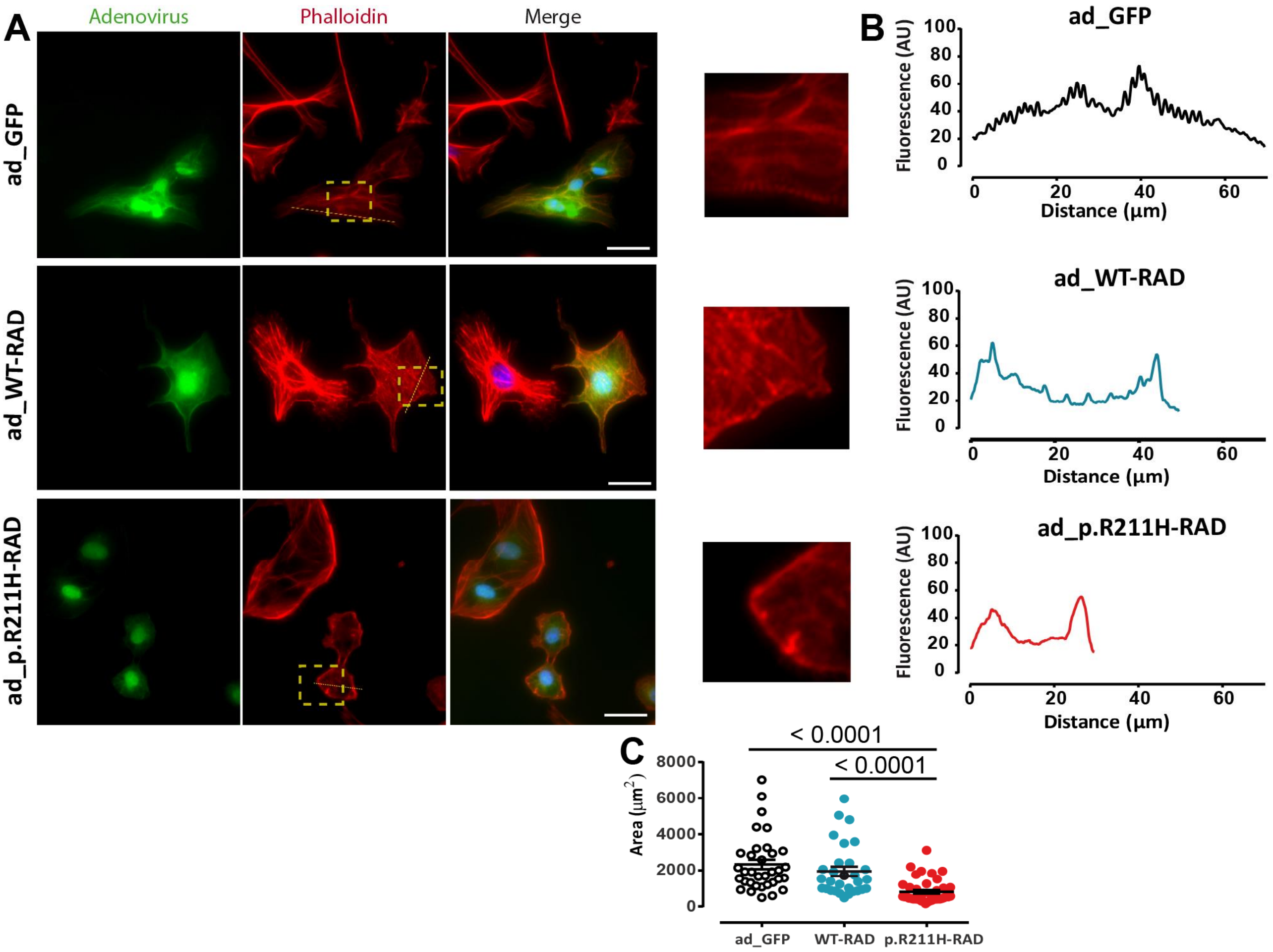

Online supplementary figure 12